The Arctic Low-Level Mixed-Phase Haze Regime and its Microphysical Differences to Mixed-Phase Clouds

Manuel Moser[1], Christiane Voigt[1,2], Oliver Eppers[3], Johannes Lucke[1,4,10], Elena De La Torre Castro[1], Johanna Mayer[1], Regis Dupuy[5], Guillaume Mioche[5], Olivier Jourdan[5], Hans-Christian Clemen[3], Johannes Schneider[3], Philipp Joppe[2,3], Stephan Mertes[6], Bruno Wetzel[6], Stephan Borrmann[2,3], Marcus Klingebiel[7], Mario Mech[8], Christof Lüpkes[9], Susanne Crewell[8], André Ehrlich[7], Andreas Herber[9], and Manfred Wendisch[7]

[1]Institut für Physik der Atmosphäre, Deutsches Zentrum für Luft- und Raumfahrt, Weßling, Germany
[2]Institut für Physik der Atmosphäre, Johannes Gutenberg-Universität, Mainz, Germany
[3]Max Planck Institute for Chemistry, Mainz, Germany
[4]Faculty of Aerospace Engineering, Delft University of Technology, Delft, Netherlands
[5]Laboratoire de Météorologie Physique, Université Clermont Auvergne, Clermont-Ferrand, France
[6]Leibniz–Institut für Troposphärenforschung, Leipzig, Germany
[7]Leipziger Institut für Meteorologie, Universität Leipzig, Leipzig, Germany
[8]Institut für Geophysik und Meteorologie, Universität zu Köln, Cologne, Germany
[9]Alfred–Wegener–Institut, Helmholtz–Zentrum für Polar– und Meeresforschung, Bremerhaven, Germany
[10]Rail Tec Arsenal, Vienna 1210, Austria

Correspondence: Manuel Moser (manuel.moser@dlr.de)

Abstract. A comprehensive in-situ dataset of low-level Arctic clouds was collected in the Fram Strait during the HALO-(AC)[3] campaign in spring 2022 using the research aircraft Polar 6. The clouds observed at altitudes below 1000 m were frequently in a mixed-phase state. We demonstrate that despite comparable optical properties, classic mixed-phase clouds (MPC) and mixed-phase haze (MPH) can be distinguished on the basis of their microphysical properties. While the thermodynamic phases

5 of the particles within the MPH are similar to those in the MPC, the supercooled droplets observed in MPC are replaced by large (> 3 µm) wet aerosol particles in MPH. Furthermore, the particle number concentration measured in MPH is reduced by approximately 3 orders of magnitude compared to MPC. MPH is observed in subsaturated air with respect to water, suggesting that the small liquid particles are haze droplets and are in equilibrium below the activation threshold to form cloud droplets. Chemical analysis suggested that the haze particles contained significant amounts of sea salt. Additional in-situ measurements

10 with an optical particle counter indicated that their number concentration was two times larger over the sea ice compared to the open ocean. Furthermore, measurements of the vertical distribution of the thermodynamic phases in low-level Arctic clouds revealed a characteristic structure, with a liquid regime frequently occurring at the top of the atmospheric boundary layer, followed by MPCs, and an MPH layer below.

The findings from this study enhance our understanding of the microphysical composition of clouds in mixed-phase condi-

15 tions.

1

1 Introduction

Over the past few decades, the Arctic region has drastically changed in response to global warming (Jeffries et al., 2013; IPCC, 2021). The accelerated warming observed at high latitudes, with a rate that is more than twice as fast as the global average (Overland et al., 2019), is known as Arctic amplification (Serreze and Francis, 2006; Wendisch et al., 2023a). Projections show that even under current efforts to mitigate greenhouse gas emissions, the Arctic will be transformed beyond contemporary recognition (Stroeve et al., 2025). Many factors influencing Arctic amplification are discussed (Wendisch et al., 2023a), including the reduction of albedo due to the decrease of the mean sea ice extent (Budyko, 1969; Sellers, 1969; Druckenmiller et al., 2022), the change in lapse rate (Pithan and Mauritsen, 2014), and changes of large scale weather patterns (Francis and Vavrus, 2012; Mann et al., 2017; Coumou et al., 2018; Kretschmer et al., 2018; Heukamp et al., 2023). The amplification is likely to be driven by a combination of multiple factors. Clouds may play a key role in the processes underlying the intense mean temperature rise at high latitudes (Wendisch et al., 2019). Low-level clouds in the Arctic are often found in a mixed-phase state (Shupe et al., 2006; Morrison et al., 2011), representing a three-phase non-equilibrium system consisting of water vapor, ice particles, and coexisting supercooled liquid water droplets. These cloud systems can persist in a quasi-steady state due to continuous water supply driven by local dynamical processes (Morrison et al., 2011). Together with stratiform liquid water clouds, Arctic mixed-phase clouds are important contributors to the Arctic surface radiation budget (Shupe and Intrieri, 2004; Wendisch et al., 2023b). In particular, the size, shape, and thermodynamic phase of the cloud particles influence the atmospheric energy fluxes and are often poorly represented in observations and models (Naud et al., 2014; Bodas-Salcedo et al., 2016; McCoy et al., 2016; Tan and Storelvmo, 2019; Wendisch et al., 2019; Kretzschmar et al., 2020; Marsing et al., 2023), contributing to the limited confidence in quantifying the cloud feedback in the Arctic climate system (Morrison et al., 2011; Bock et al., 2020; IPCC, 2021).

Several studies have investigated Arctic mixed-phase clouds using in-situ measurements, including those by McFarquhar et al. (2007), Lawson and Zuidema (2009), Klingebiel et al. (2015), Young et al. (2016), Mioche et al. (2017), Järvinen et al. (2023) and Moser et al. (2023b). These studies analyzed the microphysical processes of mixed-phase clouds and their vertical structure, examined their persistence and the influence of meteorological conditions on cloud properties, and suggested microphysical cloud parameterizations for models. However, most low-level in-situ cloud studies apply specific cloud thresholds, e.g. in liquid water content, or number concentration, that may have excluded optically thin clouds. For instance, Kirschler et al. (2022), Kirschler et al. (2023), and Sorooshian et al. (2023) defined cloud periods based on cloud water content exceeding 0.01 - 0.02 $\mathrm{g\,m^{-3}}$ and a particle number concentration greater than 10 - 20 $\mathrm{cm^{-3}}$. Similarly, Young et al. (2016) distinguished in-cloud and out-of-cloud observations using a threshold of 0.01 $\mathrm{g\,m^{-3}}$. Such thresholds may lead to the omission of thin clouds, despite their potential importance in the atmospheric radiation budget. Wendisch et al. (2013) show that the radiative forcing of low-level clouds with optical depths below 2 are particularly sensitive to small changes in optical thickness. Costa et al. (2017) observed a low number concentration ($N < 1\,\mathrm{cm^{-3}}$) in some cloud types when analysing a large in-situ data set of clouds in the mixed-phase temperature range. They have hypothesised that these clouds may have been formed by the drying of mixed-phase clouds via the Wegener-Bergeron-Findeisen process.

50   In this study, we conduct a detailed investigation of this cloud regime, which we call mixed-phase haze, characterized by relatively low particle number concentrations, analyzing its microphysical properties and differentiating it from classic mixed-phase clouds.

The article is structured as follows. Section 2 introduces the HALO-(AC)[3] field campaign, describes the instrumentation for the in-situ measurements as well as the data processing methods, and presents the prevailing environmental and meteo-

55   rological conditions together with complementary dropsonde data. Section 3 introduces the mixed-phase haze cloud regime and compares its microphysical properties with those of classic mixed-phase clouds, analyzes the chemical composition and particle number concentration of the haze droplets, and investigates the vertical distribution of cloud thermodynamic phases in the Arctic atmospheric boundary layer. Section 4 summarizes the main findings and discusses their implications.

2   Methods

2.1   The aircraft field campaign HALO-(AC)[3]

60

The HALO-(AC)[3] field campaign, conducted in March and April 2022, was a comprehensive effort to observe and analyze air mass transformations during warm-air intrusions (WAIs) and cold-air outbreaks (CAOs) over the Norwegian and Greenland Seas, the Fram Strait, and the central Arctic Ocean (Wendisch et al., 2025). The campaign utilized three research aircraft: The High Altitude and Long Range Research Aircraft (HALO; Krautstrunk and Giez, 2012; Stevens et al., 2019), operated by the

65   German Aerospace Center (DLR), and the Polar 5 and Polar 6 aircraft (Wesche et al., 2016), operated by the German Alfred Wegener Institute. At the same time, similar flight experiments were conducted in partially close proximity by the British Facility for Airborne Atmospheric Measurements (FAAM) and the French Avions de Transport Régional (ATR) aircraft. All aircraft operated in coordination, covering a broad range of altitudes and spatial scales. An overview and detailed description of the HALO-(AC)[3] field campaign is provided by Wendisch et al. (2024). A comprehensive description of the data collected

70   on board the aircraft can be found in Ehrlich et al. (2025).

This study focuses on the data collected by the Polar 6 aircraft. It is a modern version of the former Douglas DC-3, which had been modified by Basler Turbo Conversions for operations in extreme polar conditions (BT-67; Wesche et al., 2016). It was equipped with in-situ instrumentation to analyze cloud and aerosol particles. The research flights were conducted from Longyearbyen (LYR; 78° N, 15° E) in the region of the Fram Strait between Greenland and Svalbard. The flight strategy fol-

75   lowed a similar approach as applied during the previous campaigns AFLUX and MOSAiC-ACA (Mech et al., 2022a), focusing on in-situ cloud measurements in the atmospheric boundary layer over the sea ice and the open ocean. The Polar 6 flight plans included horizontal flight legs at different altitudes through clouds, as well as vertical profile measurements involving climbs or descents along a straight trajectory through cloud layers (Mech et al., 2022a). During HALO-(AC)[3], Polar 6 was temporally and spatially coordinated with HALO and Polar 5 to enable collocated in-situ and remote sensing observations, expanding on

80   similar approaches employed during the ACLOUD field campaign (Ehrlich et al., 2019; Wendisch et al., 2019).

The region where the in-situ measurements were conducted is shown in Fig. 1. The figure also displays the sea ice concentration (SIC) from satellite observations by the Advanced Microwave Scanning Radiometer 2 (AMSR2) instrument (Spreen et al.,

2008), at a representative time for the campaign (30 March 2022). The microphysical low-level cloud dataset from Polar 6

consists of a total of 19.4 h (< 1000 m, and cloud threshold CWC $> 2 \times 10^{-4}$ g m^{-3} according to Moser et al., 2023b), collected

85 during 13 flights in March and April 2022.
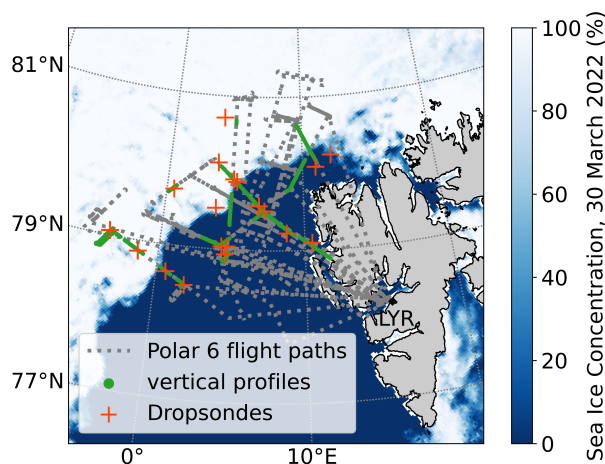
Figure 1. The map shows the region where in-situ cloud measurements were conducted with the Polar 6 aircraft. The green markers indicate the positions of vertical profiles. Orange crosses represent the locations of dropsondes collocated with the in-situ measurements used in this study. The background displays the sea ice concentration at the midpoint (30 March 2022) of the campaign, as recorded by the Advanced Microwave Scanning Radiometer 2 (AMSR2).

2.2 Cloud and aerosol in-situ instrumentation and the data processing

The Polar 6 aircraft was equipped with an advanced payload for in-situ instruments to detect cloud particles across the size range typically found in Arctic low-level clouds. For the smallest particles, between 3 μm and 50 μm, a Cloud Droplet Probe (CDP; Lance et al., 2010) scattering instrument was used to determine the particle sizes. Larger particles were measured

90 using optical array probes, specifically the Cloud Imaging Probe (CIP; Baumgardner et al., 2001) for particle diameters between 15 μm and 960 μm, and the Precipitation Imaging Probe (PIP; Baumgardner et al., 2001) for particle diameters ranging from 100 μm to 6.4 mm. By combining the data from these three instruments, a size spectrum of cloud particles, covering a range from 3 μm to 6.4 mm was established. The data processing to derive microphysical parameters such as N, effective diameter (D_{eff}), cloud water content (CWC), liquid water content (LWC), and ice water content (IWC) followed the same

95 methodology as described by Moser et al. (2023b) and Mech et al. (2022a). In addition, aerosol instruments complemented particle measurements below the detectable size range of the cloud probes. An optical particle counter (Grimm Sky-OPC, model 1.129; Heim et al., 2008; Bundke et al., 2015) measured the size distribution and concentration of aerosol particles in the size range between 0.25 and 40 μm by analyzing the scattered light as particles pass through a laser beam. However,

the upper size limit of the OPC was reduced to approximately 6 µm during HALO-(AC)[3] due to the transmission efficiencies of the inlet system and the sampling lines to the instrument. Furthermore, the single particle mass spectrometer ALABAMA (Aircraft-based Laser ABlation Aerosol MAss spectrometer; Brands et al., 2011; Köllner et al., 2017; Clemen et al., 2020) analyzed the chemical composition of individual aerosol particles in real time using laser-induced desorption/ ionization mass spectrometry. The size range of the ALABAMA ranged between 230 nm and 3 µm with 50 % detection efficiency (Clemen et al., 2020). The recorded mass spectra from the measurements conducted during the HALO-(AC)[3] flights were processed and classified into 37 clusters referring to different particle types (Ehrlich et al., 2025). Clusters containing sodium chloride (NaCl) signals were merged together to a 'sea spray' particle type. Besides the chemical composition, also the sizes of the individual particles are measured by the ALABAMA using the scattering signal at two consecutive detection laser stages. Both instruments, the OPC and the ALABAMA, were mostly operated behind the Counterflow Virtual Impactor (CVI) inlet (Ehrlich et al., 2025). The CVI enabled sampling of cloud particle residues, which remain after evaporation or sublimation of cloud droplets or ice crystals, respectively, by separating cloud particles from aerosol particles using a counterflow within the inlet system. Outside clouds, the CVI was used as particle and trace gas inlet by switching off the counterflow. In this study, only aerosol measurements outside of clouds were considered. The transmission efficiency of the inlet lines to the ALABAMA and the OPC was near unity for particles from 50 nm to about 1 µm and reduced to 80 % at 2 µm, 10 % at 4 µm and 0 % at 6 µm.

In this paper, two methodological approaches are applied based on different types of flight patterns to investigate mixed-phase conditions. First, in Sect. 3.1 we analyze and compare the microphysical properties of mixed-phase haze and mixed-phase clouds, as well as the chemical composition of the aerosol particles, with high statistical accuracy. For this purpose, only the in-situ data from the horizontal flight legs are used. Second, the thermodynamic phases are investigated in relation to environmental conditions (Sect. 3.1.2) and normalized altitude (Sect. 3.2). In this analysis, vertical flight legs, i.e., straight ascents and descents through the cloud layer, are used to characterize the vertical distribution of cloud properties. This approach is applied to correlate in-situ aircraft data with dropsonde measurements. The results from measurements conducted on vertical flight legs are statistically less significant than those from horizontal legs, however, phase determination at 1 Hz frequency, can be applied here. Additionally, during ascent and descent, different airflow conditions may affect the isocinetic sampling of the instruments, potentially leading to an increased measurement uncertainty (Moser et al., 2023b). However, previous studies have demonstrated that vertical analyses with in-situ cloud measurements are feasible (Mioche et al., 2017; Taylor et al., 2019; Schima et al., 2022; Järvinen et al., 2023; Braga et al., 2025).

By Moser et al. (2023b), a method was introduced for determining the thermodynamic phase in low-level Arctic clouds based on microphysical characteristics. The approach involves plotting 1 Hz cloud data in N - D_{eff} space, where visible clusters can be linked to specific cloud regimes including liquid, aerosol, mixed-phase, or ice regimes. This method was validated using the Polar Nephelometer and is applied here. However, in the spring data from Moser et al. (2023b), cloud particles smaller than 50 µm were measured with a Cloud Aerosol Spectrometer (CAS), which is slightly more sensitive to small particles (Braga et al., 2017). As a result, determining the thresholds for the individual regimes using the same procedure as in Moser et al. (2023b) leads to slightly different thresholds of the regimes. In this study, the thresholds of the individual regimes are extended to include at least 80 % of the data (D_{eff} and N values between the 10th and 90th percentiles) from the respective regime data

peak in the D_{eff} - N space from the HALO-(AC)[3] in-situ dataset. Although these thresholds are not substantially different from
those presented in Moser et al. (2023b), they are necessary to optimize the cloud dataset assigned to a specific thermodynamic
cloud phase. Table 1 lists the upper and lower limits of N and D_{eff} that define the respective regimes. When a data point falls
within a specific regime, the cloud thermodynamic phase is derived as follows: Regimes 1a and 1b correspond to ice particles,
regimes 2a and 2b, as we show in Sect. 3.1, to mixed-phase haze particles, regime 2c to the classic mixture of liquid water and
ice particles, regime 3 to liquid water particles, and regime 4 is associated with aerosols.

Table 1. Classification of different cloud regimes based on the in-situ measured N and D_{eff}.

Regime	Thermodynamic phase	Lower limit N	Upper limit N	Lower limit D_{eff}	Upper limit D_{eff}
1a	Ice	$10\,\mathrm{m^{-3}}$	$196\,\mathrm{m^{-3}}$	0.4 mm	2.7 mm
1b	Ice	$513\,\mathrm{m^{-3}}$	$1.9\times10^{4}\,\mathrm{m^{-3}}$	0.34 mm	2.4 mm
2a	MPH	$6.1\times10^{4}\,\mathrm{m^{-3}}$	$7.1\times10^{5}\,\mathrm{m^{-3}}$	0.15 mm	0.82 mm
2b	MPH	$6.0\times10^{4}\,\mathrm{m^{-3}}$	$4.3\times10^{5}\,\mathrm{m^{-3}}$	1.1 mm	3.6 mm
2c	MPC	$1.8\times10^{7}\,\mathrm{m^{-3}}$	$2.1\times10^{8}\,\mathrm{m^{-3}}$	0.07 mm	0.99 mm
3	Liquid	$2.4\times10^{7}\,\mathrm{m^{-3}}$	$2.5\times10^{8}\,\mathrm{m^{-3}}$	9 μm	38 μm
4	Aerosol	$6.0\times10^{4}\,\mathrm{m^{-3}}$	$4.0\times10^{5}\,\mathrm{m^{-3}}$	3 μm	10 μm

2.3 Environmental and meteorological conditions

The meteorological conditions in the Fram Strait during the HALO-(AC)[3] in-situ flights of Polar 6 were predominantly char-
acterized by CAOs. Exceptions include 20 March and 10 April, where the prevailing situations were a WAI, and 8 April, when
the meteorological condition was dominated by a polar low (Walbröl et al., 2024; Wendisch et al., 2024). Backward trajectory
analyses were conducted to determine the dominant surface type over which the low-level air masses had resided during the
24 h prior to their in-situ measurement by Polar 6. This analysis followed the same methodology as described in Moser et al.
(2023b), employing the Hybrid Single-Particle Lagrangian Integrated Trajectory model (HYSPLIT) (Stein et al., 2015; Rolph
et al., 2017) with the Global Forecast System (GFS) at a 0.25° horizontal resolution as meteorological input.

To classify the ocean surface on a daily resolution, remote sensing data from the Global Change Observation Mission-Water
(GCOM-W1) satellite were used. The AMSR2 instrument aboard the satellite recorded SIC at a spatial resolution of 3.125
km (Spreen et al., 2008). In this study, SIC values greater than 80 % are classified as sea ice, SIC values below 20 % as open
ocean, and values between 20 % and 80 % as the marginal sea ice zone (MIZ). The SIC and the derived air mass origins for
the vertical flight legs are listed in Table A1. The classification "ocean/land" indicates that the low-level air mass was mainly
influenced by the open ocean within the past 24 h. However, in some specific cases, an influence from the Svalbard land region
cannot be ruled out.

To analyze the environmental conditions of the atmosphere, profiles of temperature (T) and relative humidity with respect
to water (RH_w) measured by dropsondes were used (George et al., 2024). To calculate the relative humidity with respect to
ice (RH_{ice}), the equilibrium vapor pressure definitions provided by World Meteorological Organization (2012) are used. While

Polar 6 conducted in-situ measurements of low-level clouds, HALO and Polar 5 flew above, releasing dropsondes into the flight path of Polar 6 (Ehrlich et al., 2025). For each vertical flight profile of Polar 6, the nearest dropsonde in time and space, either launched from Polar 6 or HALO, was selected. The criteria for accepting a dropsonde to correlate with in-situ profiles were a distance of less than 70 km and a time difference of less than 2 h. In total, 33 vertical flight legs with sufficient in-situ data within and just above the atmospheric boundary layer (ABL) were flown by Polar 6. These were matched with dropsondes based on the defined criteria. The start and end times of each vertical profile from Polar 6, along with the corresponding dropsonde ID, are presented in Table A1. Meteorological data from the nose boom on Polar 6 were not used in this study due to icing conditions and associated de-icing issues, which limited the availability of reliable data to only a few days. However, these data were used to validate the correlation approach between Polar 6 and the dropsonde data. All temperature profiles from the dropsondes used in this study are shown in gray in Fig. 2. Additionally the dropsondes were classified based on satellite data to determine whether they were deployed over sea ice (SIC > 80 %), the open ocean (SIC < 20 %), or the MIZ (20 % $\leq$ SIC $\leq$ 80 %). From the measured temperature profiles of the dropsondes, the ABL height for each vertical flight leg is estimated. The ABL height is identified as the lowest altitude, at which a minimum in the temperature occurs. Additionally to the ABL height, the measured temperature at this height is provided in Table A1.
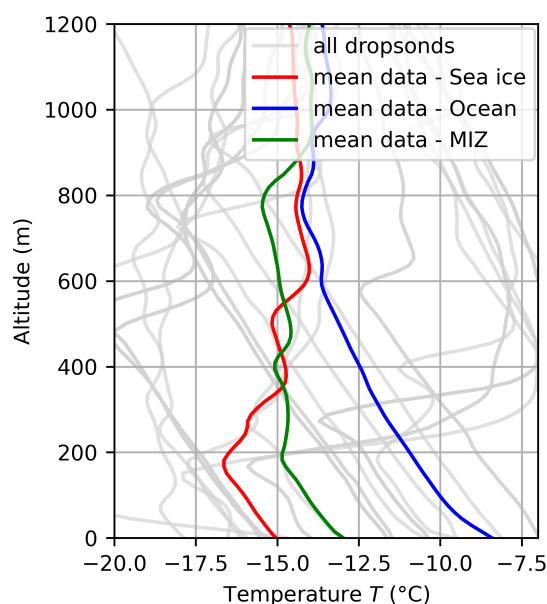
Figure 2. Temperature profiles measured by dropsondes from HALO and Polar 5. The gray lines represent all dropsondes used in the analysis in Sect. 3.1.2 and 3.2. The red line shows the averaged temperature profile from dropsondes released over sea ice, the blue line represents the averaged temperature profiles over the open ocean, and the green line corresponds to the averaged temperature profiles in the marginal sea ice zone (MIZ). All dropsondes used in this figure are listed in Table A1.

As shown in Fig. 2, the ABL height strongly depends on the underlying surface. This figure presents temperature profiles from all utilized dropsondes as a function of altitude, with mean temperature profiles over sea ice, the MIZ, and the open
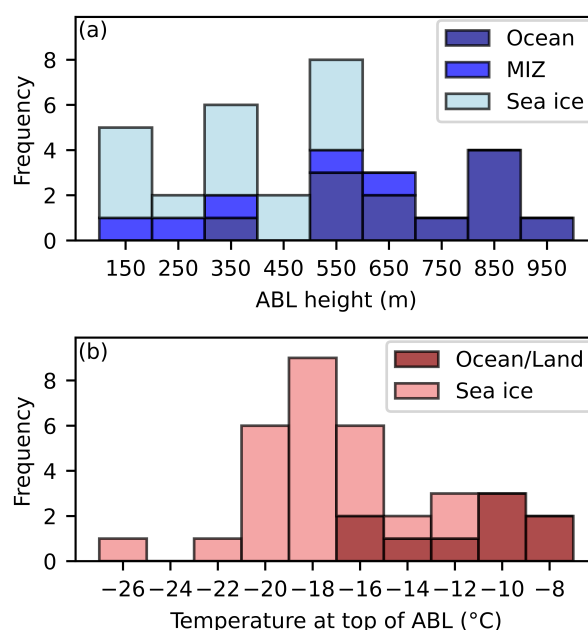
Figure 3. Data extracted from the dropsonde profiles: (a) shows the distribution of boundary layer top altitudes, color-coded by underlying surface type: Ocean, marginal ice zone, and sea ice, based on the mean sea ice concentration. (b) presents the distribution of temperatures at the top of the boundary layer, distinguished by air mass origin: 'Ocean/Land' and 'Sea ice' based on backward trajectory analyses.

ocean. The measured ABL heights and the temperatures at the ABL heights are shown as histograms in Fig. 3. While the ABL
175   is relatively shallow over sea ice and within the MIZ, it extends to significantly higher altitudes over the ocean when convection
sets in. All ABL heights below 505 m, with only one exception, were measured over sea ice or within the MIZ. Conversely,
ABL heights above 630 m were exclusively observed over the ocean. Consequently, the left part (< 500 m) of the distribution
in Fig. 3 (a) represents ABL heights over sea ice and over the MIZ, while the right part (> 600 m) corresponds to ABL heights
over the open ocean. The central peak in the histogram (at 550 m) contains ABL heights measured across all surface types.
180   Figure 3 (b) displays the distribution of temperatures measured at the ABL top. The observed temperatures range from -22°C to
-8°C, with a peak around -18°C. Based on backward trajectory analyses, all temperatures above -12°C are associated with air
masses that had interacted with either the ocean or land within the past 24 h. Conversely, for temperatures below -16.4°C, the
corresponding air masses originated from sea ice. Very similar temperature variations at the ABL top relative to air mass origin
were previously reported by Mioche et al. (2017). The analysis of Fig. 3 indicates that the vertical structure of the ABL, as
185   sampled by Polar 6, is shaped by both the underlying surface conditions and the air mass origin. While the ABL height shows
a dependence on the surface type (i.e., higher over open ocean, lower over sea ice), the temperature at the ABL top appears to
be influenced by the air mass origin. This suggests that the synoptic situation primarily determines the temperature at the top
of the ABL during HALO-(AC)[3], whereas local surface-driven processes control its vertical extent.

To consider the variable ABL height, the analyzed vertical profiles were normalized by altitude. The observed altitude, z, is normalized by the boundary layer height z_{BL}. This results in a dimensionless normalized altitude, z_{norm}, calculated as:

$$z_{\mathrm{norm}} = \frac{z}{z_{\mathrm{BL}}}, \tag{1}$$

where $z_{\mathrm{norm}} = 1$ represents the top of the boundary layer, while $z_{\mathrm{norm}} = 0$ corresponds to the surface. Values greater than 1 indicate altitudes above the boundary layer. Note that the normalized altitude applied here differs from earlier mixed-phase studies that scaled by individual cloud depth only (Mioche et al., 2017; Järvinen et al., 2023; Chechin et al., 2023).

3 Results and discussion

3.1 Microphysical properties of mixed-phase clouds and mixed-phase haze

In the following, the differences in microphysical properties between classic mixed-phase clouds and mixed-phase haze are analyzed, focusing on particle size distributions, environmental conditions, and the aerosols within the mixed-phase haze.
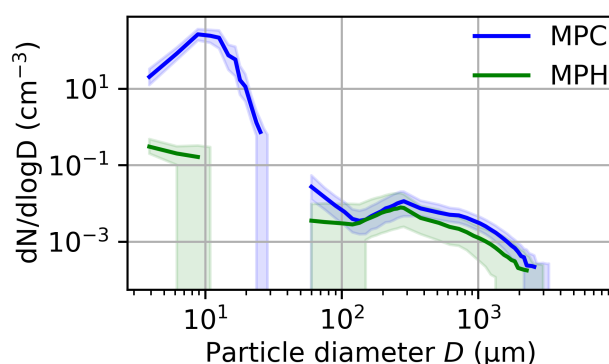
3.1.1 Particle size distribution

We analyze mixed-phase regimes (2a, 2b, 2c) by applying the phase-detection algorithm of Moser et al. (2023b) to the HALO-(AC)[3] in-situ data, focusing on their particle size distributions and microphysical composition. Regime 2c corresponds to a mixed-phase cloud typically described in literature (McFarquhar et al., 2007; Korolev et al., 2017; Morrison et al., 2011) and now will be referred to a classic mixed-phase cloud (MPC). However, in the following it is shown that the mixed-phase states, as they occur in regimes 2a and 2b, differ from a classic mixed-phase cloud, and that the term Arctic low-level mixed-phase haze or mixed-phase haze (MPH) adequately describes the regime 2a and 2b. As shown by Moser et al. (2023b) with the Polar Nephelometer, all three regimes show optical properties typical for a classic mixed-phase cloud. In terms of microphysics, however, regimes 2a and 2b differ substantially from regime 2c. The microphysical differences between regimes 2a and 2b are minor and mainly related to surface conditions (Moser et al., 2023b), while both show pronounced differences compared to regime 2c. Therefore, for the subsequent analysis, it is reasonable to combine regimes 2a and 2b into a single category representing the MPH regime, to enable a direct comparison with regime 2c (MPC).

Figure 4 presents particle size distributions (PSDs) measured under MPC (blue) and MPH (green) conditions. PSDs were calculated using data collected during horizontal flight legs below 1000 m using the combined particle measurement system. The solid lines represent the median PSDs, while the shaded areas indicate the 25th and 75th percentiles, derived from 5000 PSDs generated through bootstrapping. Each PSD was constructed from three randomly selected 1 Hz data points corresponding to the respective cloud regime. For particles larger than 50 μm, the PSD for MPC and MPH are quite similar, indicating that the size distribution of ice crystals in both regimes is comparable, as ice crystals are expected in this size range. The most significant difference between the two PSDs is observed for particles smaller than 50 μm. In classic mixed-phase clouds, the PSD shows a clear size mode between 3 μm and 30 μm caused by supercooled liquid water droplets, with a maximum at approximately 10 μm. This droplet mode is absent in the PSD of the MPH regime. Instead, the median PSD increases from

220   10 µm with decreasing size with a maximum concentration at 3 µm, which is at the lower detection limit of the CDP. Most particles in this size range are measured between 3 µm and 6 µm. The number concentration of the small particles is reduced by more than a factor of 1000 in MPH compared to MPC. It is hypothesized that, while the local maximum in the PSD of classic mixed-phase clouds (2c) is caused by supercooled liquid water droplets, the particles dominating the particle number concentration in the mixed-phase haze regimes (2a and 2b) consists of haze droplets (Hobbs and Wallace, 2006) which might

225   be dissolved sea salt particles. Consequently, we conclude that the mixed-phase haze regimes 2a and 2b consist of a mixture of small (< 6 µm) wet sea salt aerosols (SSA) and larger ice crystals. The gap in Fig. 4 between the larger ice crystals and the droplets or haze droplets arises from the low number concentration of cloud particles in this intermediate size range. The individual PSDs are computed at a frequency of 1 Hz, which is insufficient to accumulate a sufficiently large statistical sample to resolve this size range.

Figure 4. Particle size distribution of classic mixed-phase clouds (blue) and mixed-phase haze (green). Solid lines give a median value and the shaded areas represent the respective variability, calculated by the 25th and 75th percentiles.

230   The microphysical properties, including N, D_{eff}, LWC, IWC, and CWC, are summarized in Table 2 for both MPC and MPH. The microphysical values are presented for the entire PSD in the top row, followed by those for particles smaller than 50 µm (assumed to represent liquid water or haze droplets) in the middle row, and for particles larger than 50 µm (assumed to be ice particles) in the lowest row. This threshold to distinguish between liquid droplets and ice crystals is appropriate for the majority of low-level Arctic clouds (McFarquhar et al., 2007; Korolev et al., 2017). MPCs are characterized by a significantly higher

235   median particle number concentration ($\tilde{N}$) of 104.6 cm^{-3}, compared to only 0.1 cm^{-3} in MPH. This increased total number concentration in MPCs is dominated by supercooled droplets, while in MPH, $\tilde{N}$ is dominated by wet SSA, as indicated by the subsequent chemical analysis. The number concentration of ice particles is about 3 orders of magnitude smaller than the total number concentration in MPCs and about a factor of 50 smaller in MPH, making their contribution to the total number concentration negligible. The median effective diameter ($\tilde{D}_{\text{eff}}$) calculated for the entire PSD is larger in MPH with 685 µm

240   compared to MPC with 211 µm. This difference is attributed to the absence of the size mode corresponding to the supercooled droplets in MPH. The absence of this mode also leads to a slightly higher $\tilde{D}_{\text{eff}}$ for particles smaller than 50 µm in the MPH regime. However, the $\tilde{D}_{\text{eff}}$ for particles larger than 50 µm indicates that ice crystals in MPCs are larger than those in MPH

though particles > 100 μm appear to be equally represented. The CWC is calculated as the sum of liquid water content (LWC) and ice water content (IWC) (for details, see Moser et al., 2023b). The median CWC in MPCs is approximately 20 times higher than in MPH. While the CWC in MPCs is fairly evenly distributed between liquid water and ice particles, in MPH, over 99 % of the cloud water content is associated with the ice phase.

Table 2. Microphysical properties of low-level mixed-phase cloud regimes and low-level Arctic mixed-phase haze regimes: Median number concentration $\tilde{N}$, median effective diameter $\tilde{D}_{\mathrm{eff}}$ and median cloud water content $\widetilde{\mathrm{CWC}}$. The values in the square brackets give the 25th and 75th percentile, respectively. The microphysical properties are calculated from all detected cloud particles, as well as for particles smaller than 50 μm (assumed to be liquid water for mixed-phase clouds and assumed to be wet aerosols for mixed-phase haze) and for particles larger than 50 μm (assumed to be ice). The data consists of in-situ measurements during horizontal flight legs only and at altitudes below 1000 m.

	Mixed-phase cloud (MPC)	Mixed-phase haze (MPH)
$\tilde{N}$ (cm^{-3})	104.63 [57.74 / 139.24]	0.13 [0.07 / 0.25]
$\tilde{D}_{\mathrm{eff}}$ (μm)	211 [121 / 400]	685 [392 / 1445]
$\widetilde{\mathrm{CWC}}$ (g m^{-3})	0.17 [0.09 / 0.26]	(21.91 [3.87 / 244.20])×10^{-3}
$\tilde{N}_{<50\mu m}$ (cm^{-3})	104.62 [57.73 / 139.23]	0.13 [0.07 / 0.24]
$\tilde{D}_{\mathrm{eff}<50\mu m}$ (μm)	11 [10 / 13]	13 [6 / 28]
$\widetilde{\mathrm{LWC}}_{<50\mu m}$ (g m^{-3})	0.06 [0.02 / 0.11]	(0.02 [0.01 / 0.12])×10^{-3}
$\tilde{N}_{>50\mu m}$ (cm^{-3})	(11.45 [4.83 / 21.03])×10^{-3}	(2.44 [0.21 / 11.64])×10^{-3}
$\tilde{D}_{\mathrm{eff}>50\mu m}$ (μm)	1173 [879 / 1675]	747 [473 / 1479]
$\widetilde{\mathrm{IWC}}_{>50\mu m}$ (g m^{-3})	0.09 [0.05 / 0.16]	(21.52 [3.74 / 108.98])×10^{-3}

3.1.2 Influence of environmental conditions

In the following, we relate the distinct cloud microphysical properties, cloud droplets versus haze droplets, to the prevailing environmental conditions that drive the formation of the respective cloud regimes. The meteorological parameters T, RH_w, and $\mathrm{RH}_{\mathrm{ice}}$, measured in the cloud regimes classified as ice, MPH, MPC, liquid, and aerosol, are shown in Fig. 5. The data include all in-situ measurements from vertical flight profiles through the ABL that are temporally and spatially correlated with the meteorological data measured by the dropsondes (Sect. 2.3). Since mixed-phase clouds only exist at temperatures below 0 °C, all mixed-phase clouds are detected at ice supersaturated conditions. These results are in line with expectations, as classic stratiform mixed-phase clouds consist of ice particles and water droplets, with the ice crystals growing at the expense of the liquid water droplets due to water vapor deposition. A persistent Wegener-Bergeron-Findeisen process in the mixed-phase clouds implies saturation with respect to water in order to compensate the water mass transfer from the liquid water droplets to the ice crystals. Consequently, a mixed-phase is unexpected to be measured at a humidity far below saturation with respect to water, because of the short relaxation time (only a few seconds) of liquid water droplets (Korolev et al., 2017). Previous studies, such as Korolev and Isaac (2006) and Costa et al. (2017), have confirmed that the water vapor in mixed-phase clouds is close to saturation over water. Due to the greater environmental sensitivity of the liquid water phase compared to ice crystals,

pure liquid clouds display a similar distribution to that of MPCs in Fig. 5. However, liquid clouds are observed more frequently at colder temperatures, resulting in slightly higher supersaturation levels with respect to ice. For in-situ measurements of cloud regimes in absent of liquid water droplets, the ambient meteorological conditions are significantly different. The ice, aerosol, and MPH regimes are observed in notably drier conditions compared to the liquid and MPC regimes. These drier conditions

265 preclude measurements at $RH_w = 100\,\%$ in nearly all cases. However, ice and MPH regimes often display supersaturation with respect to ice, promoting the growth and persistence of ice crystals. A minor fraction of ice regimes exists in ice subsaturated conditions at $RH_{ice} < 100\,\%$, which is consistent with previous observations of ice crystals under non-equilibrium conditions (Korolev and Isaac, 2006; Voigt et al., 2017; De La Torre Castro et al., 2023; Dekoutsidis et al., 2023). Frequent observations of MPH and aerosol regimes under subsaturated conditions with respect to water support the hypothesis that the small particles

270 detected by the CDP are not cloud droplets. While ice crystals can persist in subsaturated air masses due to their extended phase relaxation time, comparable to the lifespan of an entire ice cloud (Krämer et al., 2009; Rollins et al., 2016; Korolev et al., 2017), small water droplets would evaporate immediately under such conditions. However, MPH is the most frequently observed cloud regime during the HALO-(AC)[3] campaign (see Sect.3.2) and during the AFLUX spring campaign in 2019 (Moser et al., 2023b), suggesting the presence of a stable thermodynamic condition. This thermodynamic stability of MPH in water

275 subsaturated conditions can be attributed to haze droplets composed of water and dissolved SSA. According to Köhler theory (Yau and Rogers, 1996; Laaksonen et al., 1998), these droplets achieve thermodynamic equilibrium with their surroundings at relative humidities below water saturation due to the Raoult effect. As a result, haze droplets can persist in subsaturated conditions, where pure water droplets would rapidly evaporate. Such haze droplets are often referred to as non-activated cloud droplets (Yau and Rogers, 1996; Hobbs and Wallace, 2006).

280 The size of a haze droplet is determined by the hygroscopic growth factor g_e. This factor, which represents the ratio between the radius of the haze droplet and the dry radius of the dissolved sea salt within the haze droplet, can be derived from the Köhler equation as given in Yau and Rogers (1996). Assuming the Kelvin term is negligible, the growth factor is expressed as:

$$g_e = \left(\frac{i_v M_V}{\rho_w M_S (1 - RH)} \cdot \rho_s \right)^{1/3} \tag{2}$$

with the assumptions that van't Hoff factor $i_v = 2$, molar mass of water (H_2O) $M_V = 18.02\,\mathrm{g\,mol^{-1}}$, density of water ρ_w

285 $= 1000\,\mathrm{kg\,m^{-3}}$, molar mass of the solute (NaCl) $M_S = 58.44\,\mathrm{g\,mol^{-1}}$, and density of the solute $\rho_s = 2160\,\mathrm{kg\,m^{-3}}$. With a measured median relative humidity within the MPH regime of $RH = 87.3\,\%$ (25th percentile = 84.8\,\% / 75th percentile = 92.3\,\%), the resulting hygroscopic growth factor for haze droplets in the MPH regime is 2.2 (2.1/2.6). Based on the calculated hygroscopic growth factor and the observed haze droplet sizes ranging from $3\,\mu m$ to $6\,\mu m$, the estimated dry diameter of the solute is between $1\,\mu m$ and $3\,\mu m$. Despite ambient conditions being subsaturated with respect to water, relative humidity

290 remained above the deliquescence point for NaCl ($RH_w = 74\,\%$; Zieger et al., 2017), such that sea salt particles are constantly in a dissolved state. Phase hysteresis effects including efflorescence and deliquescence are not relevant in this context (Tang et al., 1997; Zieger et al., 2017).
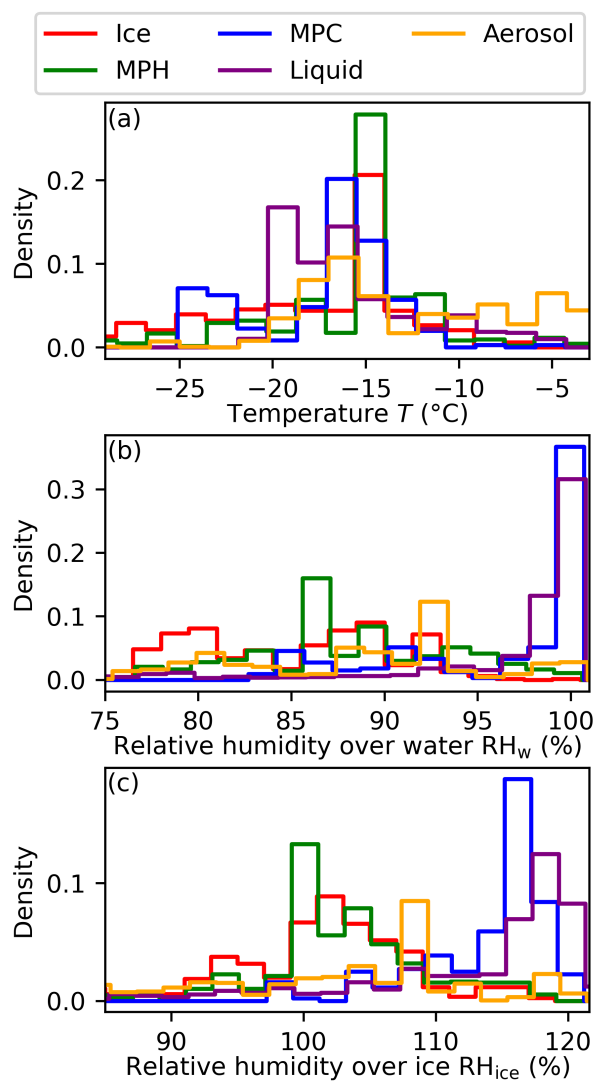
Figure 5. Normalized frequency distribution of the different cloud regimes as a function of environmental conditions such as temperature (a), relative humidity over water (b) and relative humidity over ice (c).

3.1.3 Chemical analysis and the origin of the haze particles

The microphysical description of mixed-phase haze assumes the presence of SSA in the Arctic ABL. It is well established

295 that sodium chloride (NaCl) from sea spray emission is one of the dominant locally-emitted aerosol types in the marine Arctic from late winter through spring (Kirpes et al., 2018, 2019; Chen et al., 2022; Heutte et al., 2025). This assumption is further supported by measurements from the ALABAMA instrument. Figure 6 presents the particle fraction derived from all available ALABAMA measurements below 300 m in the ABL, where the thermodynamic cloud phase classification algorithm identified either MPH or aerosol conditions. In addition, only sampling periods outside clouds were considered, as only a few cloud

300 particle residues were collected for these thin-cloud events. Figure 6 demonstrates that, in the size range above ~ 700 nm, the majority of particles are SSA. It must be considered, that the particle size obtained by the ALABAMA is given in vacuum-aerodynamic diameter (d_{va}). Assuming a shape factor for cubic or agglomerates particles and a density of $\rho_s = 2160$ kg m^{-3} for the NaCl-containing particles (Zelenyuk et al., 2006), the volume-equivalent diameter (d_{ve}) would be approximately 0.5 or 0.65 times the vacuum-aerodynamic diameter d_{va}, respectively. This would result in particles sizes in the range between

305 ~ 0.4 µm and 2 µm in terms of d_{ve} for the observed SSA. Thus, there is an overlap of the dry diameters of the haze particles from the hygroscopic growth assumption and the SSA observed by the ALABAMA. Given a relative humidity below 10% for most of the time within the sampling lines, the SSA should be crystallized arriving at the ALABAMA inlet. However, only few particles were analyzed by the ALABAMA above 3 µm, which might be due to a combination of the low transmission efficiency of the CVI inlet line and the reduced detection efficiency of the ALABAMA in this size range. Nevertheless, the

310 domination of SSA at larger particle sizes and the potential of hygroscopic growth for dry NaCl particles to sizes around 5 µm, suggest wet SSA contributing to the observed haze particles. Similar observations of large SSA have been reported in other marine boundary layer studies, highlighting that such particles can act as giant cloud condensation nuclei even outside the Arctic (Gonzalez et al., 2022). Ji et al. (2025) hypothesize that giant cloud condensation nuclei mixed within mixed-phase clouds can modify the balance between ice sublimation and droplet growth, with potential implications for the cloud's lifetime.

315 The SSA are typically found within the coarse mode of the aerosol size distribution (Lohmann et al., 2016), which cannot be fully resolved by the CDP due to its lower detection limit of 3 µm. Therefore, in the following analysis, OPC measurements are utilized to investigate the haze droplets with a particular focus on the influence of the underlying surface conditions on their properties. Previous studies have shown that over the ocean, SSA are primarily generated by wave-breaking processes (Blanchard, 1989), whereas over sea ice, mechanisms such as blowing snow or frost flowers contribute to their emission (Yang

320 et al., 2008; Seguin et al., 2014; Xu et al., 2016; Huang and Jaeglé, 2017; Willis et al., 2018; Marelle et al., 2021; Lapere et al., 2024). Figure 7 displays the boxplots of particle number concentration N (a) and effective diameter D_{eff} (b) derived from OPC measurements over the sea ice and the open ocean. Only particles with diameters exceeding 500 nm within the ABL (below 300 m) and within aerosol or mixed-phase haze conditions are considered. For each day with sufficient measurements over the sea ice and the ocean (> 100 s respectively), the data from these two surface types are displayed. The boxes labeled as "total"

325 include the data from all campaign days. A significance test is applied to assess whether the measurements over sea ice and the ocean differ significantly on a given day. The Mann-Whitney U test is performed, using a significance level of $p < 0.05$.
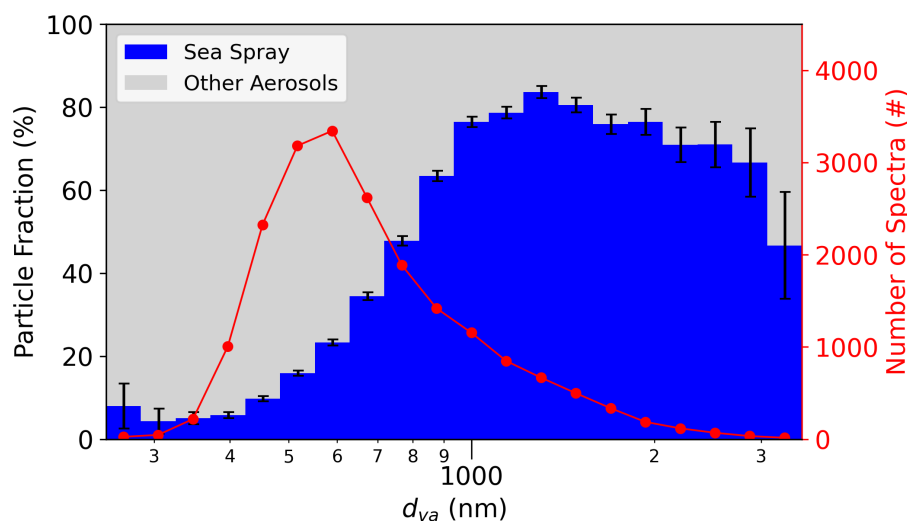
Figure 6. Number fraction of sea spray particles (blue) containing NaCl ion signals and other aerosol particles (gray) as a function of the particle size given by the vacuum-aerodynamic diameter (d_{va}). The number fraction for each logarithmic size bin was calculated with respect to the total number of spectra collected within the respective bin (red markers). The given uncertainties result from binomial statistics and are further described in Appendix B.

The data sets that have been compared are connected with a dotted line in Fig. 7. On all days except 1 April, the surface type has a significant effect on N. The effective diameter D_{eff} differs significantly between the two surfaces on six days, while no significant difference is observed on 26 March, 29 March and 9 April. In the case of N, six days show a significantly higher particle number concentration over sea ice compared to the ocean, indicating with high confidence that N is enhanced over sea ice. Only two exceptions are found: On 5 April and 10 April, N is higher over the open ocean than over sea ice. Thus, the overall OPC dataset shown as the "total" boxplot robustly represents the observed increase in N over sea ice relative to the open ocean. The measurements of D_{eff} show that on 20 March, D_{eff} is significantly higher over sea ice, whereas on five days, the D_{eff} is significantly larger over the open ocean compared to sea ice. Consequently, the total boxplot of D_{eff} represents the increase over the ocean relative to the sea ice.

Although the optical properties of MPH measured with the Polar Nephelometer indicate the presence of ice and liquid water (Moser et al., 2023b), it cannot be completely excluded that some haze droplets in MPH could be small, spherical ice crystals. However, previous in-situ aerosol measurements in the Arctic have shown that the number concentration of ice nucleating particles (INP) is mostly well below $10^4 \, \mathrm{m}^{-3}$ at temperatures higher than -20°C (Dietel et al., 2024). These measured INP number concentrations are significantly smaller (at least a factor 10, more likely a factor 10^2 - 10^5 compared to Dietel et al. (2024)) than the measured number concentrations of haze droplets in MPH. Therefore, the contribution of potentially glaciated haze droplets in MPH is negligible.

The Arctic low-level mixed-phase haze presented here is not be confused with the so-called Arctic haze. Arctic haze is a phenomenon observed predominantly in winter, characterized by high aerosol mass concentrations in the Arctic (Rahn et al.,

15
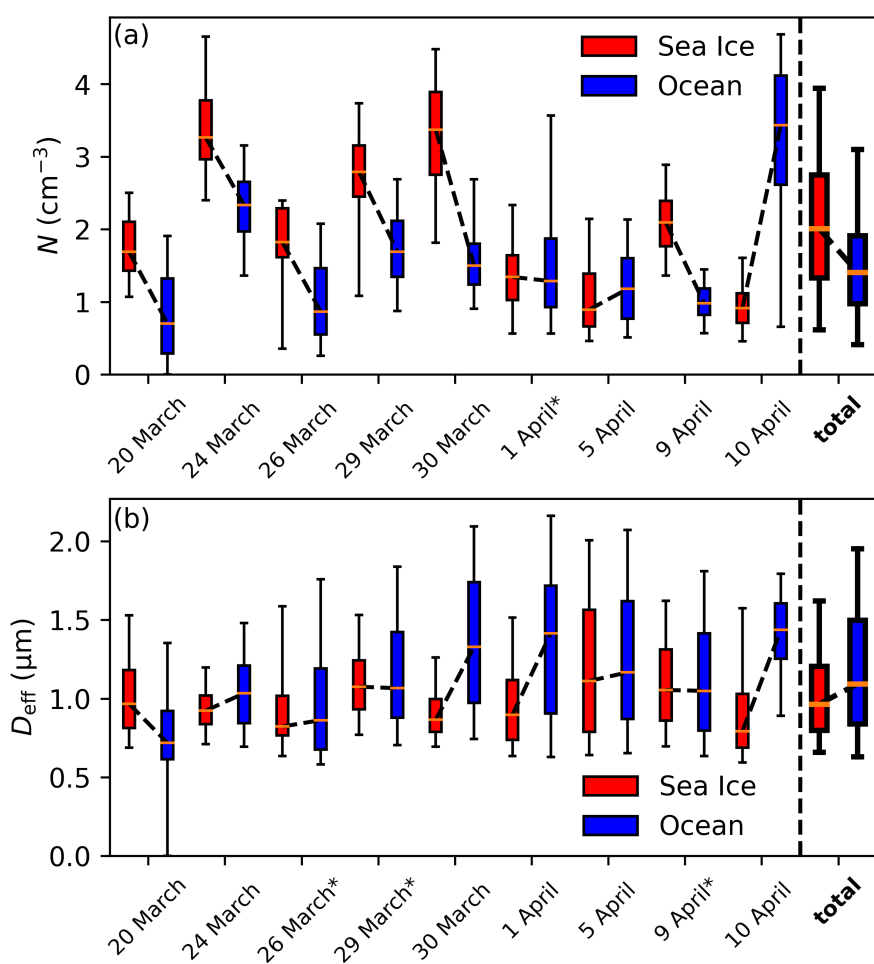
Figure 7. Overview of the N (a) and the D_{eff} (b) derived from the OPC. The boxplots include the median, upper, and lower quartiles, and the whiskers give the 5th and 95th percentile. Only particles with diameters larger 500 nm inside the ABL and during aerosol or mixed-phase haze conditions are considered. Statistically insignificant values are marked with an asterisk.

345 1977; Radke et al., 1984; Willis et al., 2018; Schmale et al., 2021). It mainly consists of aerosols from anthropogenic emissions transported over long distances from mid-latitudes to the Arctic, and is found at all altitudes in the troposphere (Quinn et al., 2007). In contrast, the haze particles investigated in this study primarily consist of SSA from local marine sources and are associated with low altitudes.
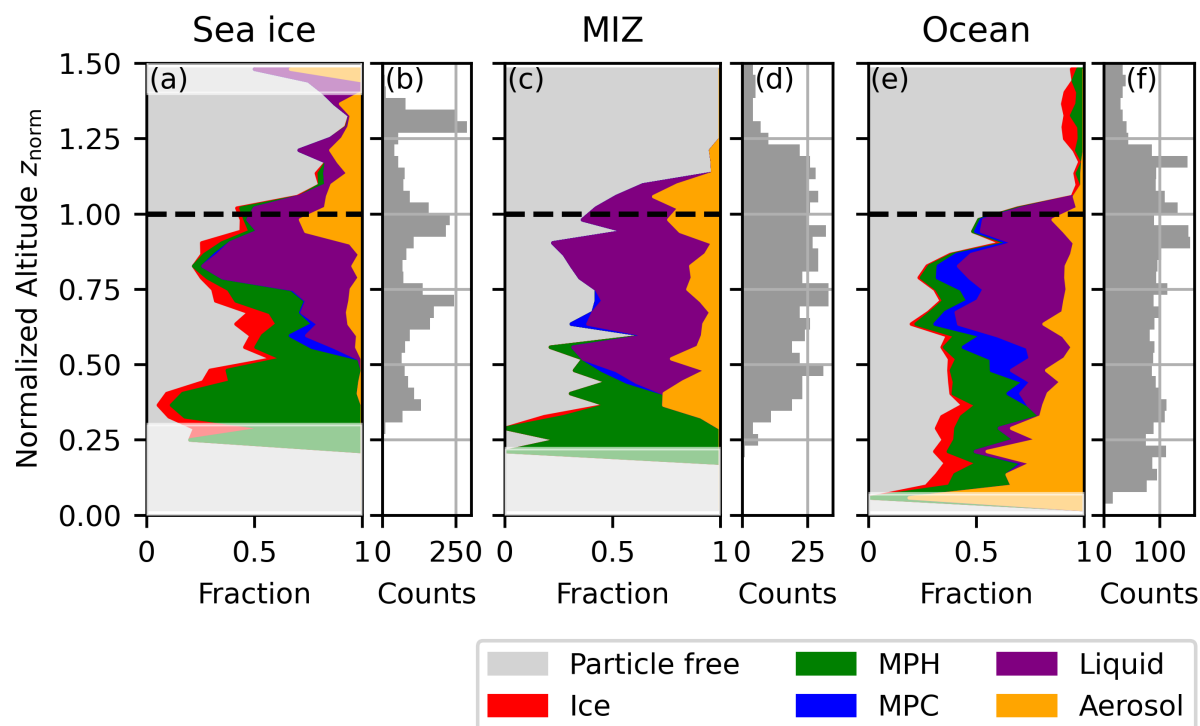
3.2 Vertical thermodynamic phase distribution of Arctic low-level clouds during HALO-(AC)[3]

350 For the analysis of the vertical distribution of thermodynamic cloud phases, all vertical flight legs with sufficient in-situ data are considered. Figure 8 presents the frequency distribution of detected thermodynamic phases in low-level cloud regimes (< 1000 m). With a frequency of 34 %, the MPH is the most common observed regime, followed by the aerosol regime with 27 % and the liquid water phase with 23 %. The ice and MPC regimes are significantly less frequent, accounting for 12 % and 4 %, respectively. This distribution of thermodynamic phases is consistent with observations of Arctic low-level mixed-phase

355 clouds during the AFLUX campaign in spring 2019 (see Fig. 9 in Moser et al., 2023b). The major differences are that fewer pure aerosol regimes were detected during AFLUX, and the pure liquid water phase was observed slightly less frequently. Despite differences in measurement strategies between AFLUX and the dataset presented in Fig. 8, as well as variations in the years of observation, the distributions align well. This consistency further supports the representativeness of this thermodynamic phase distribution for Arctic spring conditions in low-level altitude.
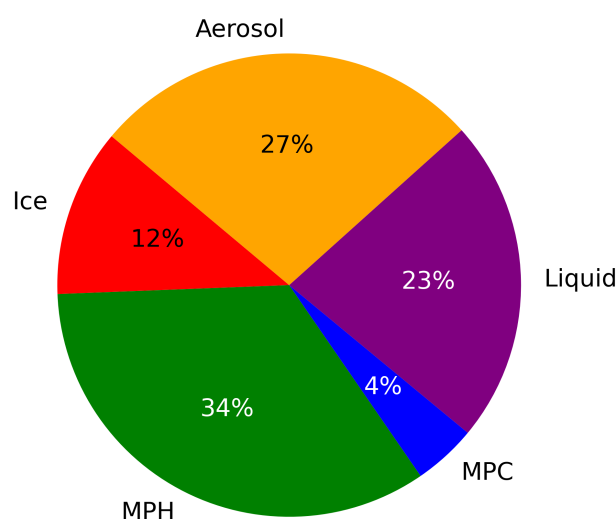
Figure 8. The fraction of different cloud regimes detected during all vertical flight legs below 1000 m during the HALO-(AC)[3] campaign.

360 Figure 9 illustrates the vertical distribution of thermodynamic cloud phases as a function of normalized altitude (Eq. 1) based on the height of the ABL for three different surface conditions. (a,b) includes all in-situ data collected from vertical flight legs over sea ice, (c,d) shows in-situ data from vertical flight legs over the MIZ, and (e,f) represents in-situ data from vertical flight legs over the ocean. Across all surface types, similar patterns in the vertical distributions can be observed. At the top of the ABL,

17

Figure 9. Distribution of the thermodynamic cloud phases derived from the in-situ cloud probe data, shown in normalized altitude. (a) shows all vertical profiles over sea ice, (c) in the marginal sea ice zone, and (e) over the open ocean. (b), (d), and (f) show the number of measurement points at the respective altitude.

clouds are most frequently in a liquid state, with pure aerosol measurements occurring less frequently than the liquid regime at
365   this altitude. Below the ABL top, the frequency of the liquid regime continues to increase in all cases, while simultaneously,
the occurrence of MPH rises with decreasing altitude. MPH becomes the dominant thermodynamic phase at lower altitudes
over sea ice and in the MIZ. The regime MPC is primarily observed in the transition region, where the dominant phase shifts
from liquid to MPH with decreasing altitude. Above the ABL top, cloud and aerosol measurements become significantly less
frequent. Some specific deviations from these general patterns are apparent. While no pure ice phase is detected in the MIZ, it
370   is consistently present throughout the entire ABL over sea ice and is observed only at lower altitudes (<0.5 normalized altitude)
over the ocean. Unlike over sea ice and the MIZ, the frequency of aerosol measurements increases with decreasing altitude over
the ocean, making aerosols the most frequently detected regime at the lowest measurement levels over the ocean. Furthermore,
it is observed that the frequency of MPCs decreases from the ocean towards the sea ice. The lower occurrence of MPCs over sea
ice compared to the open ocean has also been reported by Mioche et al. (2015, 2017). Possible explanations include the reduced
375   moisture availability over sea ice, resulting from limited updraft-driven supersaturation necessary to sustain supercooled liquid
water droplets, as well as enhanced glaciation efficiency in colder and more stable atmospheric conditions. In particular,

weak updrafts over sea ice often fail to maintain supersaturation with respect to water, causing rapid droplet evaporation under supersaturated conditions with respect to ice, whereas stronger updrafts over open ocean favor the persistence of MPCs (Korolev and Field, 2008; Costa et al., 2017). Also ice nucleating particles are expected to be less pronounced over the sea ice
380   (Dietel et al., 2024).

Compared to the 33 individual profiles analyzed in this study, the thermodynamic phase distribution shown in Figure 9 represents the overall characteristics well. In almost all individual cases, a stratification with a liquid layer at the cloud top, an MPC layer beneath it, and an MPH regime in the lower part of the cloud can be observed, consistent with the vertical thermodynamic phase pattern documented in marine cold-air outbreaks by Schirmacher et al. (2024). However, it is important
385   to note that in six individual cases, the MPH regime was detected without any liquid (liquid regime or MPC regime) layer present in the cloud profile. This suggests that the MPH regime can persist even in the absence of a liquid and MPC layer, likely resulting from the evaporation of the liquid water phase, leaving only the MPH layer behind.

As an example to illustrate the visual appearance of the MPH regime, Figure 10 (a) presents a photograph taken from the cockpit just above the cloud layer, and (b) showing the lower part of a low-level cloud layer. The vertical analysis during this
390   ascent indicates that at the time the photograph in (b) was taken, the prevailing regime was MPH. Further up in the cloud, a layer of MPC was observed, followed by a pure liquid layer at the cloud top, which is visible from above in (a). The visibility within an MPH, as seen in (b), is subjectively high, reaching up to several hundred meters. A slight haze is observed, but no whiteout conditions occur, as seen in MPC and liquid layers. Consistent with the microphysical properties, the optical thickness of MPH is significantly lower than that of MPC.
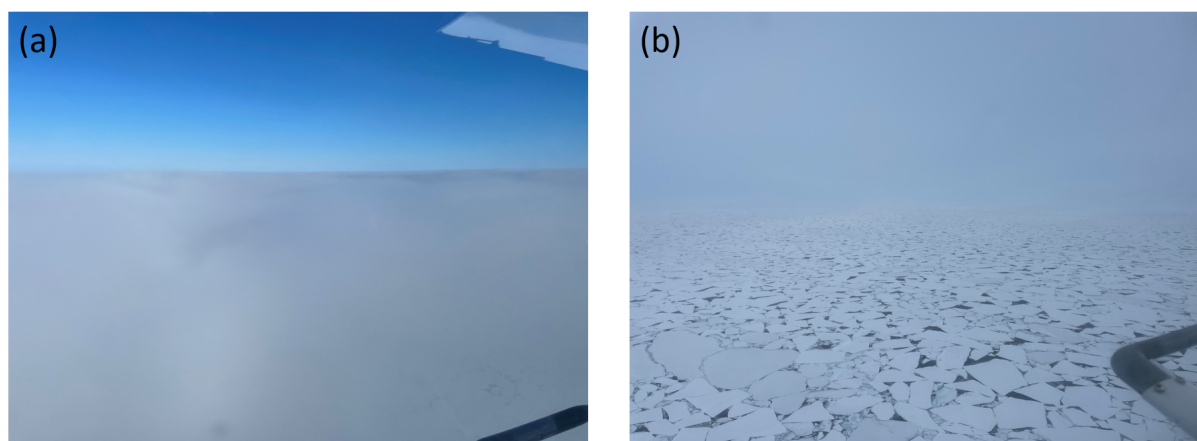
Figure 10. Pictures taken during an ascent through an Arctic low-level cloud on 10 April 2022, which consisted of an MPH regime at the bottom, an MPC regime in the middle, and a liquid layer at the cloud top. (b) was taken at 11:53 UTC within the MPH regime, while (a) was taken at 11:55 UTC just above the liquid layer.

4 Summary and conclusion

During the aircraft field campaign HALO-(AC)[3], we collected a comprehensive in-situ dataset of microphysical cloud properties below 1 km altitude above sea ice, MIZ and open ocean in the Fram Strait. A particular focus was on clouds exhibiting mixed-phase conditions. Primary results are listed below and schematically summarized in Fig. 11:

- Thermodynamic phase analyses of clouds in a mixed-phase state indicate the presence of both liquid water and ice phases. However, based on their microphysical properties, we distinguish between a classic mixed-phase cloud (MPC) and a mixed-phase haze (MPH) regime.

- While an MPC consists of a mixture of supercooled liquid water droplets and larger ice particles, the MPH is composed of unactivated haze droplets, representing solutions of water and saline aerosols, mixed with ice crystals.

- The median N and median CWC in MPCs are significantly higher compared to those in MPH, with median number concentrations increased by a factor of 1000 and cloud water content by a factor of 8. This difference is also reflected in the substantially reduced optical thickness (τ) observed for MPH.

- In MPCs, the coexistence of liquid water droplets and ice crystals requires sustained saturation with respect to water and supersaturation with respect to ice. In contrast, MPH exist in regions with $RH_w < 100\,\%$, where the persistence of haze droplets is described by unactivated cloud droplets according to the Köhler theory.

- Chemical mass spectrometric analyses identify a dominant portion of sea salt aerosols (SSA) in the size range between $0.4\,\mu m$ and $2\,\mu m$. This size range overlaps with the estimated dry diameter of the haze droplets with the assumption of NaCl composition suggesting that the observed haze droplets consist of SSA.

- Measurements with the OPC reveal a significantly increased number concentration of haze particles over the sea ice compared to the open ocean. This suggests that aerosol-generating processes over sea ice, such as blowing snow and frost flowers, contribute more to aerosol production than wave-breaking mechanisms over the ocean.

- The analysis of the vertical thermodynamic phase distribution in Arctic boundary layer clouds reveals that the most common structure follows a pattern where liquid clouds are found at the top of the ABL, followed by a classic mixed-phase cloud, and an MPH layer beneath. In some cases, pure MPH regimes without a liquid water phase are also observed within the ABL.

The findings emphasize the need of distinguishing between different types of mixed-phase regimes within Arctic boundary layer clouds. The frequency and persistence of MPH regimes imply the importance of representing this cloud regime in climate and weather models. This is essential for assessing the role of low-level clouds in the Arctic radiation budget and quantifying their feedback mechanisms in the region most affected by anthropogenic climate change.
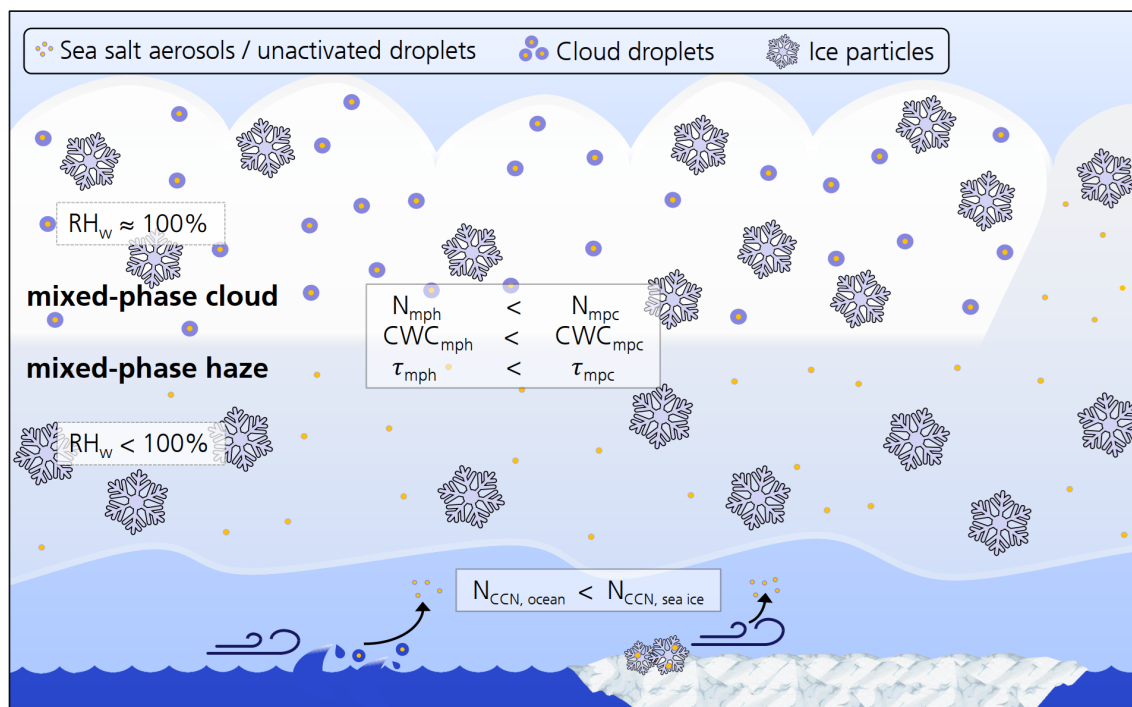
Figure 11. Summary: Schematic representation of the microphysical properties of mixed-phase haze and mixed-phase clouds.

Data availability. Processed in-situ cloud, in-situ aerosol, and dropsonde data from the HALO-(AC)[3] campaign are freely available via the
425 world data center PANGAEA (Eppers et al., 2023a, b; George et al., 2024; Moser et al., 2023a; Mertes and Wetzel, 2023). Data can be easily
reproduced and analyzed by the python package *ac3airborne* (Mech et al., 2022b) including a package for flight segmentation (Risse et al.,
2022), where each research flight is split up into logical parts like ascends, descends, specific patterns for in-situ probing, etc.. Raw in-situ
cloud data recorded by the CDP, CIP and PIP are archived at the German Aerospace Center and are available on request. Raw data by the
OPC and the ALABAMA are available from O. Eppers on request. Figures have been design with the python software Pylustrator (Gerum,
430 2020).

Author contributions. MMo conducted the analysis and wrote the manuscript. CV supervised the study and provided intensive feedback on
the manuscript. MMo, JL, EDLTC, JM, RD, GM and OJ have been responsible for the in-situ cloud probes and performed the measurements.
OE, HCC, PJ, JS, BW and SM performed the aerosol measurements during the campaign. OE and HC analyzed the ALABAMA and OPC
data. MMo, CV, JS, SB, MK, MMe, CL, SC, AE, AH, and MW conceived the flight experiments. All authors reviewed the manuscript and
435 added valuable suggestions to the final draft.

21

450   *Competing interests.* The contact author has declared that none of the authors has any competing interests.

Appendix A: Metadata for vertical profiles

Table A1. Table of flight legs, including the start and end time of each vertical flight leg, the corresponding dropsonde ID for the collocated dropsonde, the mean sea ice concentration below the flight leg, the origin of the air mass prior to measurement, the altitude of the ABL, and the temperature at the ABL height.

Start Time	End Time	Dropsonde ID	SIC (%)	Air Mass Origin	ABL Height (m)	T at ABL top (°C)
20 March 2022, 11:56:38	12:09:03	P5_RF01_01	0.0	sea ice	864	-17.15
20 March 2022, 12:10:15	12:13:00	P5_RF01_02	0.0	sea ice	665	-17.31
20 March 2022, 12:13:50	12:16:35	P5_RF01_08	22.77	sea ice	599	-17.14
20 March 2022, 12:18:42	12:21:22	P5_RF01_03	86.83	sea ice	535	-18.31
20 March 2022, 12:21:55	12:23:46	P5_RF01_03	97.54	sea ice	505	-19.51
20 March 2022, 12:24:01	12:26:14	P5_RF01_03	99.85	sea ice	479	-20.02
20 March 2022, 12:26:24	12:28:12	P5_RF01_07	98.91	sea ice	483	-20.11
20 March 2022, 12:28:21	12:29:56	P5_RF01_07	98.58	sea ice	398	-19.17
20 March 2022, 12:53:57	12:57:12	P5_RF01_05	75.94	sea ice	295	-18.27
20 March 2022, 13:44:18	13:46:13	P5_RF01_04	100.0	sea ice	379	-18.65
20 March 2022, 13:48:52	13:50:47	P5_RF01_07	99.18	sea ice	528	-20.81
20 March 2022, 13:51:02	13:53:50	P5_RF01_07	99.76	sea ice	550	-20.24
20 March 2022, 13:59:57	14:03:01	P5_RF01_08	32.89	sea ice	631	-17.37
20 March 2022, 14:03:16	14:07:44	P5_RF01_08	0.0	sea ice	850	-17.26
20 March 2022, 14:08:10	14:12:15	P5_RF01_02	0.0	sea ice	857	-16.91
20 March 2022, 14:41:58	14:45:42	P5_RF01_09	0.0	sea ice	761	-16.86
20 March 2022, 15:20:15	15:34:12	P5_RF01_12	3.14	sea ice	853	-15.83
22 March 2022, 13:54:53	13:56:11	P5_RF03_04	93.29	sea ice	186	-26.19
22 March 2022, 14:19:36	14:30:27	P5_RF03_07	14.45	sea ice	349	-22.98
29 March 2022, 14:59:48	15:10:59	P5_RF07_05	0.0	sea ice	511	-13.70
30 March 2022, 11:18:10	11:30:32	HALO_RF11_09	65.07	sea ice	183	-17.70
30 March 2022, 13:23:22	13:24:49	HALO_RF11_20	0.0	sea ice	569	-12.44
30 March 2022, 13:24:58	13:28:59	HALO_RF11_20	0.0	sea ice	581	-12.45
5 April 2022, 10:40:14	10:46:21	P5_RF11_02	0.0	ocean/land	694	-9.46
10 April 2022, 10:53:13	11:35:23	P5_RF13_14	97.08	sea ice	181	-15.72
10 April 2022, 11:42:34	11:44:56	P5_RF13_05	96.26	ocean/land	177	-16.34
10 April 2022, 11:45:05	11:46:44	P5_RF13_14	98.57	ocean/land	173	-15.89
10 April 2022, 11:48:49	11:50:32	P5_RF13_04	93.69	ocean/land	292	-13.24
10 April 2022, 11:50:47	11:53:01	P5_RF13_04	95.53	ocean/land	317	-11.66
10 April 2022, 11:53:11	11:55:18	P5_RF13_04	80.95	ocean/land	373	-7.54
10 April 2022, 11:55:33	11:57:47	P5_RF13_15	38.16	ocean/land	348	-10.38
10 April 2022, 12:06:00	12:11:10	P5_RF13_12	0.0	ocean/land	1018	-9.37
10 April 2022, 12:14:20	12:18:13	P5_RF13_11	0.0	ocean/land	937	-9.00

Appendix B: Uncertainty analysis for the particle fraction of NaCl

The absolute uncertainty of the ALABAMA particle fraction for each bin ($\sigma_{\mathrm{PF}}^{\mathrm{abs}}$) is calculated using binomial statistics (e.g., Köllner et al., 2017; Köllner et al., 2021):

455 $$\sigma_{\mathrm{PF}}^{\mathrm{abs}} = \frac{\sqrt{N_{\mathrm{hits}} \cdot \mathrm{PF} \cdot (1 - \mathrm{PF})}}{N_{\mathrm{hits}}}, \tag{B1}$$

with the number of successfully ionized particles (N_{hits}) by the desorption laser of the ALABAMA and the particle fraction of the respective particle type (PF).

References

Baumgardner, D., Jonsson, H., Dawson, W., O'Connor, D., and Newton, R.: The Cloud, Aerosol and Precipitation Spectrometer: A New
460   Instrument for Cloud Investigations, Atmospheric Research, 59–60, 251–264, https://doi.org/10.1016/S0169-8095(01)00119-3, 2001.

Blanchard, D. C.: The Ejection of Drops from the Sea and Their Enrichment with Bacteria and Other Materials: A Review, Estuaries, 12,
127, https://doi.org/10.2307/1351816, 1989.

Bock, L., Lauer, A., Schlund, M., Barreiro, M., Bellouin, N., Jones, C., Meehl, G. A., Predoi, V., Roberts, M. J., and Eyring, V.:
Quantifying Progress Across Different CMIP Phases With the ESMValTool, Journal of Geophysical Research: Atmospheres, 125,
465   https://doi.org/10.1029/2019jd032321, 2020.

Bodas-Salcedo, A., Hill, P. G., Furtado, K., Williams, K. D., Field, P. R., Manners, J. C., Hyder, P., and Kato, S.: Large Contri-
bution of Supercooled Liquid Clouds to the Solar Radiation Budget of the Southern Ocean, Journal of Climate, 29, 4213–4228,
https://doi.org/10.1175/jcli-d-15-0564.1, 2016.

Braga, R. C., Rosenfeld, D., Weigel, R., Jurkat, T., Andreae, M. O., Wendisch, M., Pöhlker, M. L., Klimach, T., Pöschl, U., Pöhlker, C., Voigt,
470   C., Mahnke, C., Borrmann, S., Albrecht, R. I., Molleker, S., Vila, D. A., Machado, L. A. T., and Artaxo, P.: Comparing parameterized
versus measured microphysical properties of tropical convective cloud bases during the ACRIDICON–CHUVA campaign, Atmospheric
Chemistry and Physics, 17, 7365–7386, https://doi.org/10.5194/acp-17-7365-2017, 2017.

Braga, R. C., Rosenfeld, D., Hernandez, D., Medcraft, C., Efraim, A., Moser, M., Lucke, J., Doss, A., and Harrison, D.: Cloud process-
ing dominates the vertical profiles of aerosols in marine air masses over the Great Barrier Reef, Atmospheric Research, 315, 107 928,
475   https://doi.org/10.1016/j.atmosres.2025.107928, 2025.

Brands, M., Kamphus, M., Böttger, T., Schneider, J., Drewnick, F., Roth, A., Curtius, J., Voigt, C., Borbon, A., Beekmann, M., Bourdon,
A., Perrin, T., and Borrmann, S.: Characterization of a Newly Developed Aircraft-Based Laser Ablation Aerosol Mass Spectrometer (AL-
ABAMA) and First Field Deployment in Urban Pollution Plumes over Paris During MEGAPOLI 2009, Aerosol Science and Technology,
45, 46–64, https://doi.org/10.1080/02786826.2010.517813, 2011.

480 Budyko, M. I.: The effect of solar radiation variations on the climate of the Earth, Tellus, 21, 611–619, https://doi.org/10.1111/j.2153-
3490.1969.tb00466.x, 1969.

Bundke, U., Berg, M., Houben, N., Ibrahim, A., Fiebig, M., Tettich, F., Klaus, C., Franke, H., and Petzold, A.: The IAGOS-CORE aerosol
package: instrument design, operation and performance for continuous measurement aboard in-service aircraft, Tellus B: Chemical and
Physical Meteorology, 67, 28 339, https://doi.org/10.3402/tellusb.v67.28339, 2015.

485 Chechin, D. G., Lüpkes, C., Hartmann, J., Ehrlich, A., and Wendisch, M.: Turbulent structure of the Arctic boundary layer in early summer
driven by stability, wind shear and cloud-top radiative cooling: ACLOUD airborne observations, Atmospheric Chemistry and Physics, 23,
4685–4707, https://doi.org/10.5194/acp-23-4685-2023, 2023.

Chen, Q., Mirrielees, J. A., Thanekar, S., Loeb, N. A., Kirpes, R. M., Upchurch, L. M., Barget, A. J., Lata, N. N., Raso, A. R. W., McNamara,
S. M., China, S., Quinn, P. K., Ault, A. P., Kennedy, A., Shepson, P. B., Fuentes, J. D., and Pratt, K. A.: Atmospheric particle abundance
490   and sea salt aerosol observations in the springtime Arctic: a focus on blowing snow and leads, Atmospheric Chemistry and Physics, 22,
15 263–15 285, https://doi.org/10.5194/acp-22-15263-2022, 2022.

Clemen, H.-C., Schneider, J., Klimach, T., Helleis, F., Köllner, F., Hünig, A., Rubach, F., Mertes, S., Wex, H., Stratmann, F., Welti, A.,
Kohl, R., Frank, F., and Borrmann, S.: Optimizing the detection, ablation, and ion extraction efficiency of a single-particle laser ablation

mass spectrometer for application in environments with low aerosol particle concentrations, Atmospheric Measurement Techniques, 13,
5923–5953, https://doi.org/10.5194/amt-13-5923-2020, 2020.

Costa, A., Meyer, J., Afchine, A., Luebke, A., Günther, G., Dorsey, J. R., Gallagher, M. W., Ehrlich, A., Wendisch, M., Baumgardner, D.,
Wex, H., and Krämer, M.: Classification of Arctic, midlatitude and tropical clouds in the mixed-phase temperature regime, Atmospheric
Chemistry and Physics, 17, 12 219–12 238, https://doi.org/10.5194/acp-17-12219-2017, 2017.

Coumou, D., Capua, G. D., Vavrus, S., Wang, L., and Wang, S.: The influence of Arctic amplification on mid-latitude summer circulation,
Nature Communications, 9, https://doi.org/10.1038/s41467-018-05256-8, 2018.

De La Torre Castro, E., Jurkat-Witschas, T., Afchine, A., Grewe, V., Hahn, V., Kirschler, S., Krämer, M., Lucke, J., Spelten, N., Wernli, H.,
Zöger, M., and Voigt, C.: Differences in microphysical properties of cirrus at high and mid-latitudes, Atmospheric Chemistry and Physics,
23, 13 167–13 189, https://doi.org/10.5194/acp-23-13167-2023, 2023.

Dekoutsidis, G., Groß, S., Wirth, M., Krämer, M., and Rolf, C.: Characteristics of supersaturation in midlatitude cirrus clouds and their
adjacent cloud-free air, Atmospheric Chemistry and Physics, 23, 3103–3117, https://doi.org/10.5194/acp-23-3103-2023, 2023.

Dietel, B., Andersen, H., Cermak, J., Stier, P., and Hoose, C.: Combined Impacts of Temperature, Sea Ice Coverage, and Mix-
ing Ratios of Sea Spray and Dust on Cloud Phase Over the Arctic and Southern Oceans, Geophysical Research Letters, 51,
https://doi.org/10.1029/2024gl110325, 2024.

Druckenmiller, M. L., Thoman, R. L., and Moon, T. A.: NOAA Arctic Report Card 2022: Executive Summary,
https://doi.org/10.25923/YJX6-R184, 2022.

Ehrlich, A., Wendisch, M., Lüpkes, C., Buschmann, M., Bozem, H., Chechin, D., Clemen, H.-C., Dupuy, R., Eppers, O., Hartmann,
J., Herber, A., Jäkel, E., Järvinen, E., Jourdan, O., Kästner, U., Kliesch, L.-L., Köllner, F., Mech, M., Mertes, S., Neuber, R., Ruiz-
Donoso, E., Schnaiter, M., Schneider, J., Stapf, J., and Zanatta, M.: A comprehensive in situ and remote sensing data set from the Arctic
CLoud Observations Using airborne measurements during polar Day (ACLOUD) campaign, Earth System Science Data, 11, 1853–1881,
https://doi.org/10.5194/essd-11-1853-2019, 2019.

Ehrlich, A., Crewell, S., Herber, A., Klingebiel, M., Lüpkes, C., Mech, M., Becker, S., Borrmann, S., Bozem, H., Buschmann, M., Clemen,
H.-C., De La Torre Castro, E., Dorff, H., Dupuy, R., Eppers, O., Ewald, F., George, G., Giez, A., Grawe, S., Gourbeyre, C., Hartmann,
J., Jäkel, E., Joppe, P., Jourdan, O., Jurányi, Z., Kirbus, B., Lucke, J., Luebke, A. E., Maahn, M., Maherndl, N., Mallaun, C., Mayer, J.,
Mertes, S., Mioche, G., Moser, M., Müller, H., Pörtge, V., Risse, N., Roberts, G., Rosenburg, S., Röttenbacher, J., Schäfer, M., Schaefer,
J., Schäfler, A., Schirmacher, I., Schneider, J., Schnitt, S., Stratmann, F., Tatzelt, C., Voigt, C., Walbröl, A., Weber, A., Wetzel, B., Wirth,
M., and Wendisch, M.: A comprehensive in situ and remote sensing data set collected during the HALO-(AC)[3] aircraft campaign, Earth
System Science Data, 17, 1295–1328, https://doi.org/10.5194/essd-17-1295-2025, 2025.

Eppers, O., Clemen, H.-C., and Schneider, J.: Aircraft-based measurement of particle size and chemical composition for individual aerosol
particles during the HALO-(AC)[3] campaign 2022, https://doi.org/10.1594/PANGAEA.963290, 2023a.

Eppers, O., Clemen, H.-C., and Schneider, J.: Airborne in-situ measurement of particle number concentration and size distribution using an
optical particle counter during HALO-(AC)[3], https://doi.org/10.1594/PANGAEA.963284, 2023b.

Francis, J. A. and Vavrus, S. J.: Evidence linking Arctic amplification to extreme weather in mid-latitudes, Geophysical Research Letters,
39, https://doi.org/10.1029/2012gl051000, 2012.

George, G., Luebke, A. E., Klingebiel, M., Mech, M., and Ehrlich, A.: Dropsonde measurements from HALO and POLAR 5 during HALO-
(AC)[3] in 2022, https://doi.org/10.1594/PANGAEA.968891, 2024.

Gerum, R.: pylustrator: code generation for reproducible figures for publication, Journal of Open Source Software, 5, 1989, https://doi.org/10.21105/joss.01989, 2020.

Gonzalez, M. E., Corral, A. F., Crosbie, E., Dadashazar, H., Diskin, G. S., Edwards, E.-L., Kirschler, S., Moore, R. H., Robinson, C. E., Schlosser, J. S., Shook, M., Stahl, C., Thornhill, K. L., Voigt, C., Winstead, E., Ziemba, L. D., and Sorooshian, A.: Relationships between supermicrometer particle concentrations and cloud water sea salt and dust concentrations: analysis of MONARC and ACTIVATE data, Environmental Science: Atmospheres, 2, 738–752, https://doi.org/10.1039/d2ea00049k, 2022.

Heim, M., Mullins, B. J., Umhauer, H., and Kasper, G.: Performance evaluation of three optical particle counters with an efficient "multi-modal" calibration method, Journal of Aerosol Science, 39, 1019–1031, https://doi.org/10.1016/j.jaerosci.2008.07.006, 2008.

Heukamp, F. O., Aue, L., Wang, Q., Ionita, M., Kanzow, T., Wekerle, C., and Rinke, A.: Cyclones modulate the control of the North Atlantic Oscillation on transports into the Barents Sea, Communications Earth & Environment, 4, https://doi.org/10.1038/s43247-023-00985-1, 2023.

Heutte, B., Bergner, N., Angot, H., Pernov, J. B., Dada, L., Mirrielees, J. A., Beck, I., Baccarini, A., Boyer, M., Creamean, J. M., Daellenbach, K. R., El Haddad, I., Frey, M. M., Henning, S., Laurila, T., Moschos, V., Petäjä, T., Pratt, K. A., Quéléver, L. L. J., Shupe, M. D., Zieger, P., Jokinen, T., and Schmale, J.: Observations of high-time-resolution and size-resolved aerosol chemical composition and microphysics in the central Arctic: implications for climate-relevant particle properties, Atmospheric Chemistry and Physics, 25, 2207–2241, https://doi.org/10.5194/acp-25-2207-2025, 2025.

Hobbs, P. V. and Wallace, J. M.: Atmospheric Science: An Introductory Survey, International geophysics series, Academic Press, San Diego, CA, 2 edn., 2006.

Huang, J. and Jaeglé, L.: Wintertime enhancements of sea salt aerosol in polar regions consistent with a sea ice source from blowing snow, Atmospheric Chemistry and Physics, 17, 3699–3712, https://doi.org/10.5194/acp-17-3699-2017, 2017.

IPCC: Climate Change 2021: The Physical Science Basis. Contribution of Working Group I to the Sixth Assessment Report of the Intergovernmental Panel on Climate Change, vol. In Press, Cambridge University Press, Cambridge, United Kingdom and New York, NY, USA, https://doi.org/10.1017/9781009157896, 2021.

Jeffries, M. O., Overland, J. E., and Perovich, D. K.: The Arctic shifts to a new normal, Physics Today, 66, 35–40, https://doi.org/10.1063/pt.3.2147, 2013.

Ji, D., Ritter, C., Sun, X., Moser, M., Voigt, C., Palm, M., and Notholt, J.: Giant Cloud Condensation Nuclei enhanced Ice Sublimation Process: A potential mechanism in mixed phase clouds, EGUsphere, 2025, 1–28, https://doi.org/10.5194/egusphere-2025-1932, 2025.

Järvinen, E., Nehlert, F., Xu, G., Waitz, F., Mioche, G., Dupuy, R., Jourdan, O., and Schnaiter, M.: Investigating the vertical extent and short-wave radiative effects of the ice phase in Arctic summertime low-level clouds, Atmospheric Chemistry and Physics, 23, 7611–7633, https://doi.org/10.5194/acp-23-7611-2023, 2023.

Kirpes, R. M., Bondy, A. L., Bonanno, D., Moffet, R. C., Wang, B., Laskin, A., Ault, A. P., and Pratt, K. A.: Secondary sulfate is internally mixed with sea spray aerosol and organic aerosol in the winter Arctic, Atmospheric Chemistry and Physics, 18, 3937–3949, https://doi.org/10.5194/acp-18-3937-2018, 2018.

Kirpes, R. M., Bonanno, D., May, N. W., Fraund, M., Barget, A. J., Moffet, R. C., Ault, A. P., and Pratt, K. A.: Wintertime Arctic Sea Spray Aerosol Composition Controlled by Sea Ice Lead Microbiology, ACS Central Science, 5, 1760–1767, https://doi.org/10.1021/acscentsci.9b00541, 2019.

Kirschler, S., Voigt, C., Anderson, B., Campos Braga, R., Chen, G., Corral, A. F., Crosbie, E., Dadashazar, H., Ferrare, R. A., Hahn, V., Hendricks, J., Kaufmann, S., Moore, R., Pöhlker, M. L., Robinson, C., Scarino, A. J., Schollmayer, D., Shook, M. A., Thornhill, K. L.,

Winstead, E., Ziemba, L. D., and Sorooshian, A.: Seasonal updraft speeds change cloud droplet number concentrations in low-level clouds over the western North Atlantic, Atmospheric Chemistry and Physics, 22, 8299–8319, https://doi.org/10.5194/acp-22-8299-2022, 2022.

Kirschler, S., Voigt, C., Anderson, B. E., Chen, G., Crosbie, E. C., Ferrare, R. A., Hahn, V., Hair, J. W., Kaufmann, S., Moore, R. H., Painemal, D., Robinson, C. E., Sanchez, K. J., Scarino, A. J., Shingler, T. J., Shook, M. A., Thornhill, K. L., Winstead, E. L., Ziemba, L. D., and Sorooshian, A.: Overview and statistical analysis of boundary layer clouds and precipitation over the western North Atlantic Ocean, Atmospheric Chemistry and Physics, 23, 10 731–10 750, https://doi.org/10.5194/acp-23-10731-2023, 2023.

Klingebiel, M., de Lozar, A., Molleker, S., Weigel, R., Roth, A., Schmidt, L., Meyer, J., Ehrlich, A., Neuber, R., Wendisch, M., and Borrmann, S.: Arctic low-level boundary layer clouds: in situ measurements and simulations of mono- and bimodal supercooled droplet size distributions at the top layer of liquid phase clouds, Atmospheric Chemistry and Physics, 15, 617–631, https://doi.org/10.5194/acp-15-617-2015, 2015.

Köllner, F., Schneider, J., Willis, M. D., Klimach, T., Helleis, F., Bozem, H., Kunkel, D., Hoor, P., Burkart, J., Leaitch, W. R., Aliabadi, A. A., Abbatt, J. P. D., Herber, A. B., and Borrmann, S.: Particulate trimethylamine in the summertime Canadian high Arctic lower troposphere, Atmospheric Chemistry and Physics, 17, 13 747–13 766, https://doi.org/10.5194/acp-17-13747-2017, 2017.

Köllner, F., Schneider, J., Willis, M. D., Schulz, H., Kunkel, D., Bozem, H., Hoor, P., Klimach, T., Helleis, F., Burkart, J., Leaitch, W. R., Aliabadi, A. A., Abbatt, J. P. D., Herber, A. B., and Borrmann, S.: Chemical composition and source attribution of sub-micrometre aerosol particles in the summertime Arctic lower troposphere, Atmos. Chem. Phys., 21, 6509–6539, 2021.

Korolev, A. and Field, P. R.: The Effect of Dynamics on Mixed-Phase Clouds: Theoretical Considerations, Journal of the Atmospheric Sciences, 65, 66–86, https://doi.org/10.1175/2007jas2355.1, 2008.

Korolev, A. and Isaac, G.: Relative Humidity in Liquid, Mixed-Phase, and Ice Clouds, Journal of The Atmospheric Sciences - J ATMOS SCI, 63, 2865–2880, https://doi.org/10.1175/JAS3784.1, 2006.

Korolev, A., McFarquhar, G., Field, P. R., Franklin, C., Lawson, R. P., Wang, Z., Williams, E., Abel, S. J., Axisa, D., Borrmann, S., Crosier, J., Fugal, J., Krämer, M., Lohmann, U., Schlenczek, O., Schnaiter, M., and Wendisch, M.: Mixed-Phase Clouds: Progress and Challenges, Meteorological Monographs, 58, 5.1–5.50, https://doi.org/10.1175/amsmonographs-d-17-0001.1, 2017.

Krämer, M., Schiller, C., Afchine, A., Bauer, R., Gensch, I., Mangold, A., Schlicht, S., Spelten, N., Sitnikov, N., Borrmann, S., de Reus, M., and Spichtinger, P.: Ice supersaturations and cirrus cloud crystal numbers, Atmospheric Chemistry and Physics, 9, 3505–3522, https://doi.org/10.5194/acp-9-3505-2009, 2009.

Krautstrunk, M. and Giez, A.: The Transition From FALCON to HALO Era Airborne Atmospheric Research, p. 609–624, Springer Berlin Heidelberg, ISBN 9783642301834, https://doi.org/10.1007/978-3-642-30183-4_37, 2012.

Kretschmer, M., Coumou, D., Agel, L., Barlow, M., Tziperman, E., and Cohen, J.: More-Persistent Weak Stratospheric Polar Vortex States Linked to Cold Extremes, Bulletin of the American Meteorological Society, 99, 49–60, https://doi.org/10.1175/bams-d-16-0259.1, 2018.

Kretzschmar, J., Stapf, J., Klocke, D., Wendisch, M., and Quaas, J.: Employing airborne radiation and cloud microphysics observations to improve cloud representation in ICON at kilometer-scale resolution in the Arctic, Atmospheric Chemistry and Physics, 20, 13 145–13 165, https://doi.org/10.5194/acp-20-13145-2020, 2020.

Laaksonen, A., Korhonen, P., Kulmala, M., and Charlson, R. J.: Modification of the Köhler Equation to Include Soluble Trace Gases and Slightly Soluble Substances, Journal of the Atmospheric Sciences, 55, 853–862, https://doi.org/10.1175/1520-0469(1998)055<0853:motkhe>2.0.co;2, 1998.

605   Lance, S., Brock, C. A., Rogers, D., and Gordon, J. A.: Water droplet calibration of the Cloud Droplet Probe (CDP) and in-
        flight performance in liquid, ice and mixed-phase clouds during ARCPAC, Atmospheric Measurement Techniques, 3, 1683–1706,
        https://doi.org/10.5194/amt-3-1683-2010, 2010.

Lapere, R., Marelle, L., Rampal, P., Brodeau, L., Melsheimer, C., Spreen, G., and Thomas, J. L.: Modeling the contribution of leads to sea
        spray aerosol in the high Arctic, Atmospheric Chemistry and Physics, 24, 12 107–12 132, https://doi.org/10.5194/acp-24-12107-2024,
610   2024.

Lawson, R. P. and Zuidema, P.: Aircraft Microphysical and Surface-Based Radar Observations of Summertime Arctic Clouds, Journal of the
        Atmospheric Sciences, 66, 3505–3529, https://doi.org/10.1175/2009jas3177.1, 2009.

Lohmann, U., Lüönd, F., and Mahrt, F.: An Introduction to Clouds: From the Microscale to Climate, Cambridge University Press,
        https://doi.org/10.1017/cbo9781139087513, 2016.

615   Mann, M. E., Rahmstorf, S., Kornhuber, K., Steinman, B. A., Miller, S. K., and Coumou, D.: Influence of Anthropogenic Climate Change
        on Planetary Wave Resonance and Extreme Weather Events, Scientific Reports, 7, https://doi.org/10.1038/srep45242, 2017.

Marelle, L., Thomas, J. L., Ahmed, S., Tuite, K., Stutz, J., Dommergue, A., Simpson, W. R., Frey, M. M., and Baladima, F.: Implementation
        and Impacts of Surface and Blowing Snow Sources of Arctic Bromine Activation Within WRF-Chem 4.1.1, Journal of Advances in
        Modeling Earth Systems, 13, https://doi.org/10.1029/2020ms002391, 2021.

620   Marsing, A., Meerkötter, R., Heller, R., Kaufmann, S., Jurkat-Witschas, T., Krämer, M., Rolf, C., and Voigt, C.: Investigating the ra-
        diative effect of Arctic cirrus measured in situ during the winter 2015–2016, Atmospheric Chemistry and Physics, 23, 587–609,
        https://doi.org/10.5194/acp-23-587-2023, 2023.

McCoy, D. T., Tan, I., Hartmann, D. L., Zelinka, M. D., and Storelvmo, T.: On the relationships among cloud cover, mixed-phase partitioning,
        and planetary albedo in GCMs, Journal of Advances in Modeling Earth Systems, 8, 650–668, https://doi.org/10.1002/2015ms000589,
625   2016.

McFarquhar, G. M., Zhang, G., Poellot, M. R., Kok, G. L., McCoy, R., Tooman, T., Fridlind, A., and Heymsfield, A. J.: Ice properties of
        single-layer stratocumulus during the Mixed-Phase Arctic Cloud Experiment: 1. Observations, Journal of Geophysical Research, 112,
        https://doi.org/10.1029/2007jd008633, 2007.

Mech, M., Ehrlich, A., Herber, A., Lüpkes, C., Wendisch, M., Becker, S., Boose, Y., Chechin, D., Crewell, S., Dupuy, R., Gourbeyre, C.,
630   Hartmann, J., Jäkel, E., Jourdan, O., Kliesch, L.-L., Klingebiel, M., Kulla, B. S., Mioche, G., Moser, M., Risse, N., Ruiz-Donoso, E.,
        Schäfer, M., Stapf, J., and Voigt, C.: MOSAiC-ACA and AFLUX - Arctic airborne campaigns characterizing the exit area of MOSAiC,
        Scientific Data, 9, https://doi.org/10.1038/s41597-022-01900-7, 2022a.

Mech, M., Risse, N., Marrollo, G., and Paul, D.: Ac3airborne, Zenodo, https://doi.org/10.5281/zenodo.7305585, 2022b.

Mertes, S. and Wetzel, B.: Airborne in-situ measurements of aerosol properties of cloud particle residuals / ambient particles and of the cloud
635   water content / water vapor during the HALO-AC3 campaign in March and April 2022, https://doi.org/10.1594/PANGAEA.963771, 2023.

Mioche, G., Jourdan, O., Ceccaldi, M., and Delanoë, J.: Variability of mixed-phase clouds in the Arctic with a focus on the Svalbard region:
        a study based on spaceborne active remote sensing, Atmospheric Chemistry and Physics, 15, 2445–2461, https://doi.org/10.5194/acp-15-
        2445-2015, 2015.

Mioche, G., Jourdan, O., Delanoë, J., Gourbeyre, C., Febvre, G., Dupuy, R., Monier, M., Szczap, F., Schwarzenboeck, A., and Gayet, J.-F.:
640   Vertical distribution of microphysical properties of Arctic springtime low-level mixed-phase clouds over the Greenland and Norwegian
        seas, Atmospheric Chemistry and Physics, 17, 12 845–12 869, https://doi.org/10.5194/acp-17-12845-2017, 2017.

Morrison, H., de Boer, G., Feingold, G., Harrington, J., Shupe, M. D., and Sulia, K.: Resilience of persistent Arctic mixed-phase clouds, Nature Geoscience, 5, 11–17, https://doi.org/10.1038/ngeo1332, 2011.

Moser, M., Lucke, J., De La Torre Castro, E., Mayer, J., and Voigt, C.: DLR in situ cloud measurements during HALO-(AC)[3] Arctic airborne

645   campaign, https://doi.org/10.1594/PANGAEA.963247, 2023a.

Moser, M., Voigt, C., Jurkat-Witschas, T., Hahn, V., Mioche, G., Jourdan, O., Dupuy, R., Gourbeyre, C., Schwarzenboeck, A., Lucke, J., Boose, Y., Mech, M., Borrmann, S., Ehrlich, A., Herber, A., Lüpkes, C., and Wendisch, M.: Microphysical and thermodynamic phase analyses of Arctic low-level clouds measured above the sea ice and the open ocean in spring and summer, Atmospheric Chemistry and Physics, 23, 7257–7280, https://doi.org/10.5194/acp-23-7257-2023, 2023b.

650   Naud, C. M., Booth, J. F., and Genio, A. D. D.: Evaluation of ERA-Interim and MERRA Cloudiness in the Southern Ocean, Journal of Climate, 27, 2109–2124, https://doi.org/10.1175/jcli-d-13-00432.1, 2014.

Overland, J., Dunlea, E., Box, J. E., Corell, R., Forsius, M., Kattsov, V., Olsen, M. S., Pawlak, J., Reiersen, L.-O., and Wang, M.: The urgency of Arctic change, Polar Science, 21, 6–13, https://doi.org/10.1016/j.polar.2018.11.008, 2019.

Pithan, F. and Mauritsen, T.: Arctic amplification dominated by temperature feedbacks in contemporary climate models, Nature Geoscience,

655   7, 181–184, https://doi.org/10.1038/ngeo2071, 2014.

Quinn, P. K., Shaw, G., Andrews, E., Dutton, E. G., Ruoho-Airola, T., and Gong, S. L.: Arctic haze: current trends and knowledge gaps, Tellus B, 59, https://doi.org/10.3402/tellusb.v59i1.16972, 2007.

Radke, L. F., Hobbs, P. V., and Bailey, I. H.: Airborne observations of Arctic aerosols. III: Origins and effects of airmasses, Geophysical Research Letters, 11, 401–404, https://doi.org/10.1029/gl011i005p00401, 1984.

660   Rahn, K. A., Borys, R. D., and Shaw, G. E.: The Asian source of Arctic haze bands, Nature, 268, 713–715, https://doi.org/10.1038/268713a0, 1977.

Risse, N., Marrollo, G., Paul, D., and Mech, M.: Ac3airborne - Flight-Phase-Separation, Zenodo, https://doi.org/10.5281/zenodo.7305558, 2022.

Rollins, A. W., Thornberry, T. D., Gao, R. S., Woods, S., Lawson, R. P., Bui, T. P., Jensen, E. J., and Fahey, D. W.: Observational con-

665   straints on the efficiency of dehydration mechanisms in the tropical tropopause layer, Geophysical Research Letters, 43, 2912–2918, https://doi.org/10.1002/2016gl067972, 2016.

Rolph, G., Stein, A., and Stunder, B.: Real-time environmental applications and display sYstem: READY, Environ. Model. Softw., 95, 210–228, 2017.

Schima, J., McFarquhar, G., Romatschke, U., Vivekanandan, J., D'Alessandro, J., Haggerty, J., Wolff, C., Schaefer, E., Järvinen, E., and

670   Schnaiter, M.: Characterization of Southern Ocean Boundary Layer Clouds Using Airborne Radar, Lidar, and In Situ Cloud Data: Results From SOCRATES, Journal of Geophysical Research: Atmospheres, 127, https://doi.org/10.1029/2022jd037277, 2022.

Schirmacher, I., Schnitt, S., Klingebiel, M., Maherndl, N., Kirbus, B., Ehrlich, A., Mech, M., and Crewell, S.: Clouds and precipitation in the initial phase of marine cold-air outbreaks as observed by airborne remote sensing, Atmospheric Chemistry and Physics, 24, 12 823–12 842, https://doi.org/10.5194/acp-24-12823-2024, 2024.

675   Schmale, J., Zieger, P., and Ekman, A. M. L.: Aerosols in current and future Arctic climate, Nature Climate Change, 11, 95–105, https://doi.org/10.1038/s41558-020-00969-5, 2021.

Seguin, A. M., Norman, A.-L., and Barrie, L.: Evidence of sea ice source in aerosol sulfate loading and size distribution in the Canadian High Arctic from isotopic analysis, Journal of Geophysical Research: Atmospheres, 119, 1087–1096, https://doi.org/10.1002/2013jd020461, 2014.

680   Sellers, W. D.: A Global Climatic Model Based on the Energy Balance of the Earth-Atmosphere System, Journal of Applied Meteorology,
         8, 392–400, https://doi.org/10.1175/1520-0450(1969)008<0392:agcmbo>2.0.co;2, 1969.

       Serreze, M. C. and Francis, J. A.: The Arctic Amplification Debate, Climatic Change, 76, 241–264, https://doi.org/10.1007/s10584-005-
         9017-y, 2006.

       Shupe, M. D. and Intrieri, J. M.: Cloud Radiative Forcing of the Arctic Surface: The Influence of Cloud Properties, Surface Albedo, and
685   Solar Zenith Angle, Journal of Climate, 17, 616–628, https://doi.org/10.1175/1520-0442(2004)017<0616:crfota>2.0.co;2, 2004.

       Shupe, M. D., Matrosov, S. Y., and Uttal, T.: Arctic Mixed-Phase Cloud Properties Derived from Surface-Based Sensors at SHEBA, Journal
         of the Atmospheric Sciences, 63, 697 – 711, https://doi.org/10.1175/JAS3659.1, 2006.

       Sorooshian, A., Alexandrov, M. D., Bell, A. D., Bennett, R., Betito, G., Burton, S. P., Buzanowicz, M. E., Cairns, B., Chemyakin, E. V., Chen,
         G., Choi, Y., Collister, B. L., Cook, A. L., Corral, A. F., Crosbie, E. C., van Diedenhoven, B., DiGangi, J. P., Diskin, G. S., Dmitrovic,
690   S., Edwards, E.-L., Fenn, M. A., Ferrare, R. A., van Gilst, D., Hair, J. W., Harper, D. B., Hilario, M. R. A., Hostetler, C. A., Jester, N.,
         Jones, M., Kirschler, S., Kleb, M. M., Kusterer, J. M., Leavor, S., Lee, J. W., Liu, H., McCauley, K., Moore, R. H., Nied, J., Notari, A.,
         Nowak, J. B., Painemal, D., Phillips, K. E., Robinson, C. E., Scarino, A. J., Schlosser, J. S., Seaman, S. T., Seethala, C., Shingler, T. J.,
         Shook, M. A., Sinclair, K. A., Smith Jr., W. L., Spangenberg, D. A., Stamnes, S. A., Thornhill, K. L., Voigt, C., Vömel, H., Wasilewski,
         A. P., Wang, H., Winstead, E. L., Zeider, K., Zeng, X., Zhang, B., Ziemba, L. D., and Zuidema, P.: Spatially coordinated airborne data and
695   complementary products for aerosol, gas, cloud, and meteorological studies: the NASA ACTIVATE dataset, Earth System Science Data,
         15, 3419–3472, https://doi.org/10.5194/essd-15-3419-2023, 2023.

       Spreen, G., Kaleschke, L., and Heygster, G.: Sea ice remote sensing using AMSR-E 89-GHz channels, Journal of Geophysical Research,
         113, https://doi.org/10.1029/2005jc003384, 2008.

       Stein, A. F., Draxler, R. R., Rolph, G. D., Stunder, B. J. B., Cohen, M. D., and Ngan, F.: NOAA's HYSPLIT atmospheric transport and
700   dispersion modeling system, Bull. Am. Meteorol. Soc., 96, 2059–2077, 2015.

       Stevens, B., Ament, F., Bony, S., Crewell, S., Ewald, F., Gross, S., Hansen, A., Hirsch, L., Jacob, M., Kölling, T., Konow, H., Mayer, B.,
         Wendisch, M., Wirth, M., Wolf, K., Bakan, S., Bauer-Pfundstein, M., Brueck, M., Delanoë, J., Ehrlich, A., Farrell, D., Forde, M., Gödde,
         F., Grob, H., Hagen, M., Jäkel, E., Jansen, F., Klepp, C., Klingebiel, M., Mech, M., Peters, G., Rapp, M., Wing, A. A., and Zinner,
         T.: A High-Altitude Long-Range Aircraft Configured as a Cloud Observatory: The NARVAL Expeditions, Bulletin of the American
705   Meteorological Society, 100, 1061–1077, https://doi.org/10.1175/bams-d-18-0198.1, 2019.

       Stroeve, J. C., Notz, D., Dawson, J., Schuur, E. A. G., Dahl-Jensen, D., and Giesse, C.: Disappearing landscapes: The Arctic at +2.7°C global
         warming, Science, 387, 616–621, https://doi.org/10.1126/science.ads1549, 2025.

       Tan, I. and Storelvmo, T.: Evidence of Strong Contributions From Mixed-Phase Clouds to Arctic Climate Change, Geophysical Research
         Letters, 46, 2894–2902, https://doi.org/10.1029/2018gl081871, 2019.

710   Tang, I. N., Tridico, A. C., and Fung, K. H.: Thermodynamic and optical properties of sea salt aerosols, Journal of Geophysical Research:
         Atmospheres, 102, 23 269–23 275, https://doi.org/10.1029/97jd01806, 1997.

       Taylor, J. W., Haslett, S. L., Bower, K., Flynn, M., Crawford, I., Dorsey, J., Choularton, T., Connolly, P. J., Hahn, V., Voigt, C., Sauer, D.,
         Dupuy, R., Brito, J., Schwarzenboeck, A., Bourriane, T., Denjean, C., Rosenberg, P., Flamant, C., Lee, J. D., Vaughan, A. R., Hill, P. G.,
         Brooks, B., Catoire, V., Knippertz, P., and Coe, H.: Aerosol influences on low-level clouds in the West African monsoon, Atmospheric
715   Chemistry and Physics, 19, 8503–8522, https://doi.org/10.5194/acp-19-8503-2019, 2019.

       Voigt, C., Schumann, U., Minikin, A., Abdelmonem, A., Afchine, A., Borrmann, S., Boettcher, M., Buchholz, B., Bugliaro, L., Costa, A.,
         Curtius, J., Dollner, M., Dörnbrack, A., Dreiling, V., Ebert, V., Ehrlich, A., Fix, A., Forster, L., Frank, F., Fütterer, D., Giez, A., Graf,

K., Grooß, J.-U., Groß, S., Heimerl, K., Heinold, B., Hüneke, T., Järvinen, E., Jurkat, T., Kaufmann, S., Kenntner, M., Klingebiel, M., Klimach, T., Kohl, R., Krämer, M., Krisna, T. C., Luebke, A., Mayer, B., Mertes, S., Molleker, S., Petzold, A., Pfeilsticker, K., Port, M.,
720   Rapp, M., Reutter, P., Rolf, C., Rose, D., Sauer, D., Schäfler, A., Schlage, R., Schnaiter, M., Schneider, J., Spelten, N., Spichtinger, P., Stock, P., Walser, A., Weigel, R., Weinzierl, B., Wendisch, M., Werner, F., Wernli, H., Wirth, M., Zahn, A., Ziereis, H., and Zöger, M.: ML-CIRRUS: The Airborne Experiment on Natural Cirrus and Contrail Cirrus with the High-Altitude Long-Range Research Aircraft HALO, Bulletin of the American Meteorological Society, 98, 271–288, https://doi.org/10.1175/bams-d-15-00213.1, 2017.

Walbröl, A., Michaelis, J., Becker, S., Dorff, H., Ebell, K., Gorodetskaya, I., Heinold, B., Kirbus, B., Lauer, M., Maherndl, N., Maturilli, M.,
725   Mayer, J., Müller, H., Neggers, R. A. J., Paulus, F. M., Röttenbacher, J., Rückert, J. E., Schirmacher, I., Slättberg, N., Ehrlich, A., Wendisch, M., and Crewell, S.: Contrasting extremely warm and long-lasting cold air anomalies in the North Atlantic sector of the Arctic during the HALO-(AC)[3] campaign, Atmospheric Chemistry and Physics, 24, 8007–8029, https://doi.org/10.5194/acp-24-8007-2024, 2024.

Wendisch, M., Yang, P., and Ehrlich, A.: Amplified climate changes in the arctic: Role of clouds and atmospheric radiation, Hirzel, S., Verlag, Stuttgart, Germany, 1 edn., 2013.

730   Wendisch, M., Macke, A., Ehrlich, A., Lüpkes, C., Mech, M., Chechin, D., Dethloff, K., Velasco, C. B., Bozem, H., Brückner, M., Clemen, H.-C., Crewell, S., Donth, T., Dupuy, R., Ebell, K., Egerer, U., Engelmann, R., Engler, C., Eppers, O., Gehrmann, M., Gong, X., Gottschalk, M., Gourbeyre, C., Griesche, H., Hartmann, J., Hartmann, M., Heinold, B., Herber, A., Herrmann, H., Heygster, G., Hoor, P., Jafariserajehlou, S., Jäkel, E., Järvinen, E., Jourdan, O., Kästner, U., Kecorius, S., Knudsen, E. M., Köllner, F., Kretzschmar, J., Lelli, L., Leroy, D., Maturilli, M., Mei, L., Mertes, S., Mioche, G., Neuber, R., Nicolaus, M., Nomokonova, T., Notholt, J., Palm, M., van Pinxteren,
735   M., Quaas, J., Richter, P., Ruiz-Donoso, E., Schäfer, M., Schmieder, K., Schnaiter, M., Schneider, J., Schwarzenböck, A., Seifert, P., Shupe, M. D., Siebert, H., Spreen, G., Stapf, J., Stratmann, F., Vogl, T., Welti, A., Wex, H., Wiedensohler, A., Zanatta, M., and Zeppenfeld, S.: The Arctic Cloud Puzzle: Using ACLOUD/PASCAL Multiplatform Observations to Unravel the Role of Clouds and Aerosol Particles in Arctic Amplification, Bulletin of the American Meteorological Society, 100, 841–871, https://doi.org/10.1175/bams-d-18-0072.1, 2019.

Wendisch, M., Brückner, M., Crewell, S., Ehrlich, A., Notholt, J., Lüpkes, C., Macke, A., Burrows, J. P., Rinke, A., Quaas, J., Maturilli,
740   M., Schemann, V., Shupe, M. D., Akansu, E. F., Barrientos-Velasco, C., Bärfuss, K., Blechschmidt, A.-M., Block, K., Bougoudis, I., Bozem, H., Böckmann, C., Bracher, A., Bresson, H., Bretschneider, L., Buschmann, M., Chechin, D. G., Chylik, J., Dahlke, S., Deneke, H., Dethloff, K., Donth, T., Dorn, W., Dupuy, R., Ebell, K., Egerer, U., Engelmann, R., Eppers, O., Gerdes, R., Gierens, R., Gorodetskaya, I. V., Gottschalk, M., Griesche, H., Gryanik, V. M., Handorf, D., Harm-Altstädter, B., Hartmann, J., Hartmann, M., Heinold, B., Herber, A., Herrmann, H., Heygster, G., Höschel, I., Hofmann, Z., Hölemann, J., Hünerbein, A., Jafariserajehlou, S., Jäkel, E., Jacobi, C., Janout,
745   M., Jansen, F., Jourdan, O., Jurányi, Z., Kalesse-Los, H., Kanzow, T., Käthner, R., Kliesch, L. L., Klingebiel, M., Knudsen, E. M., Kovács, T., Körtke, W., Krampe, D., Kretzschmar, J., Kreyling, D., Kulla, B., Kunkel, D., Lampert, A., Lauer, M., Lelli, L., von Lerber, A., Linke, O., Löhnert, U., Lonardi, M., Losa, S. N., Losch, M., Maahn, M., Mech, M., Mei, L., Mertes, S., Metzner, E., Mewes, D., Michaelis, J., Mioche, G., Moser, M., Nakoudi, K., Neggers, R., Neuber, R., Nomokonova, T., Oelker, J., Papakonstantinou-Presvelou, I., Pätzold, F., Pefanis, V., Pohl, C., van Pinxteren, M., Radovan, A., Rhein, M., Rex, M., Richter, A., Risse, N., Ritter, C., Rostosky, P., Rozanov, V. V.,
750   Donoso, E. R., Saavedra Garfias, P., Salzmann, M., Schacht, J., Schäfer, M., Schneider, J., Schnierstein, N., Seifert, P., Seo, S., Siebert, H., Soppa, M. A., Spreen, G., Stachlewska, I. S., Stapf, J., Stratmann, F., Tegen, I., Viceto, C., Voigt, C., Vountas, M., Walbröl, A., Walter, M., Wehner, B., Wex, H., Willmes, S., Zanatta, M., and Zeppenfeld, S.: Atmospheric and Surface Processes, and Feedback Mechanisms Determining Arctic Amplification: A Review of First Results and Prospects of the (AC)3 Project, Bulletin of the American Meteorological Society, 104, E208–E242, https://doi.org/10.1175/bams-d-21-0218.1, 2023a.

755   Wendisch, M., Stapf, J., Becker, S., Ehrlich, A., Jäkel, E., Klingebiel, M., Lüpkes, C., Schäfer, M., and Shupe, M. D.: Effects of variable ice–ocean surface properties and air mass transformation on the Arctic radiative energy budget, Atmospheric Chemistry and Physics, 23, 9647–9667, https://doi.org/10.5194/acp-23-9647-2023, 2023b.

Wendisch, M., Crewell, S., Ehrlich, A., Herber, A., Kirbus, B., Lüpkes, C., Mech, M., Abel, S. J., Akansu, E. F., Ament, F., Aubry, C., Becker, S., Borrmann, S., Bozem, H., Brückner, M., Clemen, H.-C., Dahlke, S., Dekoutsidis, G., Delanoë, J., De La Torre Castro, E., Dorff, H., 760   Dupuy, R., Eppers, O., Ewald, F., George, G., Gorodetskaya, I. V., Grawe, S., Groß, S., Hartmann, J., Henning, S., Hirsch, L., Jäkel, E., Joppe, P., Jourdan, O., Jurányi, Z., Karalis, M., Kellermann, M., Klingebiel, M., Lonardi, M., Lucke, J., Luebke, A. E., Maahn, M., Maherndl, N., Maturilli, M., Mayer, B., Mayer, J., Mertes, S., Michaelis, J., Michalkov, M., Mioche, G., Moser, M., Müller, H., Neggers, R., Ori, D., Paul, D., Paulus, F. M., Pilz, C., Pithan, F., Pöhlker, M., Pörtge, V., Ringel, M., Risse, N., Roberts, G. C., Rosenburg, S., Röttenbacher, J., Rückert, J., Schäfer, M., Schaefer, J., Schemann, V., Schirmacher, I., Schmidt, J., Schmidt, S., Schneider, J., Schnitt, S., 765   Schwarz, A., Siebert, H., Sodemann, H., Sperzel, T., Spreen, G., Stevens, B., Stratmann, F., Svensson, G., Tatzelt, C., Tuch, T., Vihma, T., Voigt, C., Volkmer, L., Walbröl, A., Weber, A., Wehner, B., Wetzel, B., Wirth, M., and Zinner, T.: Overview: quasi-Lagrangian observations of Arctic air mass transformations – introduction and initial results of the HALO-(AC)[3] aircraft campaign, Atmospheric Chemistry and Physics, 24, 8865–8892, https://doi.org/10.5194/acp-24-8865-2024, 2024.

Wendisch, M., Kirbus, B., Ori, D., Shupe, M. D., Crewell, S., Sodemann, H., and Schemann, V.: Observed and modeled Arctic airmass 770   transformations during warm air intrusions and cold air outbreaks, EGUsphere, 2025, 1–42, https://doi.org/10.5194/egusphere-2025-2062, 2025.

Wesche, C., Steinhage, D., and Nixdorf, U.: Polar aircraft Polar5 and Polar6 operated by the Alfred Wegener Institute, Journal of large-scale research facilities JLSRF, 2, https://doi.org/10.17815/jlsrf-2-153, 2016.

Willis, M. D., Leaitch, W. R., and Abbatt, J. P.: Processes Controlling the Composition and Abundance of Arctic Aerosol, Reviews of 775   Geophysics, 56, 621–671, https://doi.org/10.1029/2018rg000602, 2018.

World Meteorological Organization: Guide to Meteorological Instruments and Methods of Observation, 2008 edition updated 2010., WMO, https://doi.org/10.25607/OBP-1528, 2012.

Xu, L., Russell, L. M., and Burrows, S. M.: Potential sea salt aerosol sources from frost flowers in the pan-Arctic region, J. Geophys. Res., 121, 10,840–10,856, 2016.

780   Yang, X., Pyle, J. A., and Cox, R. A.: Sea salt aerosol production and bromine release: Role of snow on sea ice, Geophysical Research Letters, 35, https://doi.org/10.1029/2008gl034536, 2008.

Yau, M. K. and Rogers, R. R.: A short course in cloud physics, Elsevier, 1996.

Young, G., Jones, H. M., Choularton, T. W., Crosier, J., Bower, K. N., Gallagher, M. W., Davies, R. S., Renfrew, I. A., Elvidge, A. D., Darbyshire, E., Marenco, F., Brown, P. R. A., Ricketts, H. M. A., Connolly, P. J., Lloyd, G., Williams, P. I., Allan, J. D., Taylor, J. W., 785   Liu, D., and Flynn, M. J.: Observed microphysical changes in Arctic mixed-phase clouds when transitioning from sea ice to open ocean, Atmospheric Chemistry and Physics, 16, 13 945–13 967, https://doi.org/10.5194/acp-16-13945-2016, 2016.

Zelenyuk, A., Cai, Y., and and, D. I.: From Agglomerates of Spheres to Irregularly Shaped Particles: Determination of Dynamic Shape Factors from Measurements of Mobility and Vacuum Aerodynamic Diameters, Aerosol Science and Technology, 40, 197–217, https://doi.org/10.1080/02786820500529406, 2006.

790   Zieger, P., Väisänen, O., Corbin, J. C., Partridge, D. G., Bastelberger, S., Mousavi-Fard, M., Rosati, B., Gysel, M., Krieger, U. K., Leck, C., Nenes, A., Riipinen, I., Virtanen, A., and Salter, M. E.: Revising the hygroscopicity of inorganic sea salt particles, Nature Communications, 8, https://doi.org/10.1038/ncomms15883, 2017.